

Accretion onto Proca stars

José Carlos Olvera M.

December 2021

Resumen

Los agujeros negros pueden distinguirse de otros objetos compactos debido a la presencia de un horizonte de eventos que desconecta causalmente la región interna con el exterior. Sin embargo, hay objetos compactos (algunos de naturaleza exótica) que pueden imitar algunas características observacionales de agujeros negros. Trabajos recientes apuntan a que un objeto importante en este contexto, son las estrellas de Proca, ya que se ajustan a algunas observaciones de ondas gravitacionales y pueden imitar la sombra de un agujero negro. Para obtener una forma de distinguir estos objetos, se debe considerar otro enfoque. En este trabajo se estudia el problema de acreción en dichos objetos por medio de un análisis de la evolución de las propiedades magnetohidrodinámicas del disco de acreción, para encontrar diferencias cualitativas y cuantitativas en el comportamiento del flujo de acreción de ambos objetos.

Abstract

Black holes can be distinguished from other compact objects due the presence of an event horizon which causally disconnects the inner region from the exterior. However, there are compact objects (some from exotic nature) that can imitate some observational properties of black holes. Recent works point out that an important object, regarding these imitators, are Proca stars, as they adjust better to some gravitational wave signatures and can also mimic the shadow of a black hole. In order to obtain a way to distinguish these objects, another approach must be considered. This work studies the problem of accretion onto these compact objects through an analysis of the evolution of magnetohydrodynamic properties from the accretion disk in order to find qualitative and quantitative differences in the behaviour of the accretion flow between both objects.

Contents

1. Introduction	4
2. Astrophysical Observations of Strong Gravity	6
2.1. Observations	6
2.1.1. Gravitational waves	6
2.1.2. Shadows of compact objects	7
2.2. Detectors and Telescopes	8
2.2.1. Laser Interferometry	9
2.2.2. Very Long Baseline Interferometry (VLBI)	10
3. Numerical relativity and general relativistic magnetohydrodynamics	11
3.1. 3+1 formulation	11
3.1.1. Foliations and hypersurfaces	11
3.1.2. ADM/York evolution equations	14
3.2. General Relativistic Magnetohydrodynamics	17
3.2.1. GRMHD equations	17
3.2.2. Valencia Formulation	20
3.2.3. Hyperbolic structure and Riemann problem	22
3.3. Numerical Methods	23
3.3.1. Finite volume formulation and High resolution shock capturing schemes	24
3.3.2. Reconstruction techniques	26
3.3.3. Riemann solvers	27
3.3.4. Time update	28
3.4. GRMHD codes	28

3.4.1. Computational implementation of GRMHD equations . . .	29
3.4.2. Black Hole Accretion Code (BHAC)	32
4. Compact objects	34
4.1. The physics of black holes and compact objects	34
4.2. Schwarzschild Black Holes	35
4.3. Boson stars	37
4.4. Proca Stars	39
4.5. Boson and Proca stars as black hole mimickers	42
5. Accretion	46
5.1. Accretion flows around compact objects	46
5.2. Magnetorotational instability	48
5.3. Thick tori as initial condition	49
6. Numerical simulations of Accretion onto Proca stars	53
6.1. Physical configuration	53
6.2. Computational and numerical configuration	56
6.3. Results	61
7. Discussion and Conclusions	64
8. Appendix A: Cauchy problem and hyperbolic systems	66
8.1. Partial differential equations and the Cauchy problem	66

1. Introduction

Recent observations of the compact object's shadow at the center of the M87 galaxy by the Event Horizon Telescope Collaboration (EHTC) [9] and the first detection of gravitational waves (GW) on 2015 by LIGO [1] allow for a new way to study and gain insight about objects such as black holes (BHs), which arise from Einstein's general relativity (GR). These and other global collaborations along with the new generation of detectors and telescopes, reaffirmed the value of Einstein's theory and opened the way for theories of gravity which needed testing, such as nonlinear electrodynamics [10, 70], modified gravity [53], dark matter [41, 73, 72] and even more fundamental theories and results [52, 109, 24].

However, although several observations have been made regarding the possibility of black holes, it is not certain whether event horizons can be distinguished by observations [6] and there are some other astrophysical and theoretical objects which fulfill the compactness requirement, and can act as "horizonless" BH mimickers [75]. These imitators exhibit a similar same behaviour, in the astrophysical context, as spacetimes that represent black holes. Objects such as wormholes [84], gravastars [31], boson stars [54], and more recently, Proca stars [25], can be mistaken for a BH, as their observational signature would produce similar results due to their extreme gravity.

New studies from gravitational waves suggest that other compact objects, of exotic nature, may be relevant to study in the case of inspiral binaries [131], and that in some cases, the exotic nature adjusts better to the observations, such as the signal from GW190521, which is highly consistent with numerical simulated signals coming from a Proca star merger [25].

As for the shadow's observation of M87 [9], it is known that shadows cast by BHs can also be degenerate [66] or theoretically equivalent to other compact objects. A recent analysis shows that static Proca stars can mimic a Schwarzschild shadow [59]. This evidence raises more questions as if the massive object observed by the EHT, really represents a Kerr BH.

One way to distinguish black holes from these objects is to study the near-horizon related effects and to try to recreate the results obtained by the EHTC, LIGO, and other observations, which will, at least, raise significant constraints on the nature of the mimickers [65]. Work in this direction has been done for wormholes [90], gravastars [32] and boson stars [96], which makes it possible to tell the differences between such objects and BHs. However, there is not enough information about Proca stars in this context, which is the aim of this work.

Another useful approach to study compact objects is to analyze the effects produced by the object's geometry in their surroundings by means of an accretion disk, which can be seen as an orbiting halo of matter [104]. This approach

has the particularity that the model can be extended to include as many interactions as possible, such as magnetic fields, self-gravity, etc.[3].

Similarities between Proca stars and BHs have been also studied in the context of gravitational lensing [59], however, the observational results are completely dependent on the angle of observation, which can produce an observational degeneration, causing the possible differences between both objects, to not be apparent or directly visible. This result forces other approaches to be studied in order to be able to distinguish between a Proca star and a black hole.

This work is organized as follows: Chapter 2 presents a brief introduction to astrophysical observations and how these are obtained. The mathematical and physical background to understand GRMHD equations, as well as the numerical methods applied to solve them and analyse them, is contained on Chapter 3. Chapter 4 introduces the compact objects that are relevant to this work and establishes the physics behind them, while Chapter 5 contains a brief review of the accretion processes relevant to the physics of compact objects. The essence of this work is presented in Chapter 6, where the numerical results from this work, as well as the procedure followed to obtain them, are discussed. Finally the conclusions and future perspectives along this line of research are shown.

2. Astrophysical Observations of Strong Gravity

Since the first mention of general relativity, a variety of techniques have been developed in order to observe and obtain information regarding phenomena studied under this theory. These techniques are useful to confirm the predictions from general relativity and to provide data used in the study of alternate theories of gravity. This chapter describes the most relevant techniques and observables studied in order to obtain information about the regime of strong gravity in the context of black hole mimickers.

2.1. Observations

2.1.1. Gravitational waves

The study of the strong regime of gravity consisted on observations of the effects present in electromagnetic radiation due to the gravitational effects, however, in 2015, the first gravitational wave was observed by the Laser Interferometer Gravitational-wave Observatory (LIGO), opening a new window into the study of the universe. Since then, multiple observations of these waves have been made.

Gravitational waves are oscillations of spacetime itself due to the acceleration of massive objects. They can be defined as a low-frequency propagation of spacetime distortions associated to mass and as such, they do not interact with matter in a significant way, in contrast with electromagnetic waves, which represent the propagation of the electromagnetic fields through spacetime and usually are either absorbed or scattered by matter due to their typically higher frequency (higher with respect to gravitational waves).

As gravitational waves interact weakly with matter, when they reach Earth, they carry most of the information regarding the event that produced such radiation. This results in a weaker, but cleaner signal than the ones obtained from electromagnetic radiation, which is altered due to the numerous radiation sources distributed over the intergalactic medium. Another important difference between electromagnetic and gravitational radiation can be found when studying the theoretical foundations of both theories, specifically, the multipole expansion, as for gravitational radiation, the quadrupole term is dominant [78].

Gravitational waves are characterized by two independent polarization modes, which are related to the motion of the source, as well as the orientation, and in the case of rotating systems, the polarization carries information about the axis of rotation.

The amplitude and frequency of the gravitational waves are key constraints for the waves to be detected due to detector limitations. Such factors are determined by the nature of the phenomena that produces the radiation.

Amplitude is directly related to the distance to the source and the intrinsic strength of the interaction. On the other hand, frequency is related to the mass of the source, however, this dependence is not the same for all systems, for example, a simple self-gravitating system depends directly on the mass, while for a binary system, it is the rate of change of the frequency which depends on the mass, but not directly, instead through a function known as chirp mass [116].

Typical sources of gravitational radiation involve [21, 79]:

- Binary systems: Systems composed by two orbiting bodies. Such bodies can be black holes, neutron or other compact stars.
- Supernovas.
- Individual rotating stars.
- Supermassive black holes.

2.1.2. Shadows of compact objects

Another important observable in the study of compact objects, are the shadows. The observation of the shadow of a compact object consists in studying the deflection of light, produced by the gravitational influence of the object, and is also known as gravitational lensing, which is a technique that has been used widely in the last decades. Light, when subjected to gravitational influence, propagates along null geodesics, which are not always straight paths due to the spacetime curvature [37]. These paths of light can often create the optical effect of a shadow due to the fact that photons can stay in orbit around a compact object only in a certain range of distances from the center.

Shadows corresponding to different spacetimes can not always be distinguished, and this can be due to either theoretical effects, such as a mathematical degeneration in the calculation of the shadow, as shown in [66], or observational problems regarding resolution.

Shadows and light rings can also be present in ultra-compact objects, however, they are stable only for brief periods of time, making them easily distinguishable from black holes [27, 39]. Around some compact objects that present no surface (such as boson and Proca stars), apparent shadows can appear due to different astrophysical effects that take place in the environment. Even in black holes, these effects are usually important and modify the shape

of the shadow in a significant way. A full description of the problem requires to take into account general relativistic magnetohydrodynamics (GRMHD) and the radiative processes that occur into the system.

The study of idealized shadows of compact objects makes two suppositions. The first one consists in considering that there is no light nor matter between the object and the observer, making the radiation arrive unperturbed from the source and the second assumption consists in not considering the effects from accretion related process around the object. The first issue is usually improved by implementing ray tracing, such as discussed in [100]. The second issue, as mentioned before, is studied by means of GRMHD simulations.

The first observation of the shadow of a compact object took place in 2017 by the Event Horizon Telescope Collaboration [9]. This observation consisted in mapping the compact object located at the center of the galaxy M87. The results are consistent with the theoretical predictions of a Kerr black hole with mass of $(6.5 \pm 0.7) \times 10^9 M_\odot$ rotating in clockwise direction, however, in order to be certain about the nature of the compact object observed by the EHT, it is necessary to explore all possibilities.

The other possibilities considered in the case of the object from M87, are subdivided into three categories by the EHT collaboration [8]:

- Black hole solutions from the standard Einstein equations that include additional fields.
- Black hole solutions from alternative or extended theories of gravity.
- Compact objects that appear as black hole mimickers, usually stars composed from exotic matter.

More observations and simulations are needed regarding these possibilities in order to confirm the nature of the object.

2.2. Detectors and Telescopes

This section deals with a brief description of the detectors and techniques (based on interferometry) that are commonly used in the study of gravity, specifically, regarding the study of gravitational waves, (which are studied with the use of laser interferometry, to detect the very small oscillations produced through spacetime) and shadows of compact objects (which need very long baseline interferometry in order to create images with enough resolution to distinguish these objects from the intergalactic background).

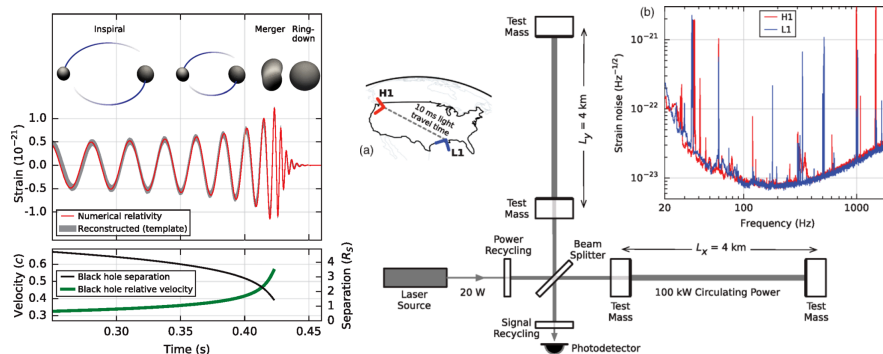


Figure 1: First panel: The first observation of the gravitational wave event GW150914, showing the basic anatomy of a classical gravitational wave signal as seen through the strain produced by each phase of the process. Left panel: Diagram of the LIGO detector showing the signal from GW150914 in the frequency domain [1].

2.2.1. Laser Interferometry

Interferometry consists in obtaining information through the observation of interference patterns and is now the most relevant method to obtain information about gravitational waves [101]. The first and most basic interferometer, known as Michelson-Morley interferometer, consisted in a beam of coherent source of light going through a beam splitter, which separates the beam into two orthogonal directions that return to the splitter after being reflected in a mirror. The paths followed by the beams are in vacuum, such that when the beams return, they will interfere without a change in phase, however, the final pattern can show interference and this is due to one of the light rays being intercepted by a signal. The phase difference that results in the interference pattern is related to the length of the arms (or the distance that the photons travel). In order to maximize the phase difference of a typical gravitational wave in a LIGO-type interferometer, the length of each arm must be of approximately 750 km [78].

This, however, is not a realistic situation, and in order to solve the problem, Fabry-Perot cavities are implemented. The interaction of gravitational waves with Fabry-Perot cavities is discussed in [126]. This method consists in aligning two parallel highly reflective mirrors such that they allow for light to travel farther in a shorter distance. The implementation of these cavities allows LIGO-type interferometers to maximize the phase difference with arms of only 4 km.

The laser beam present in the LIGO detector is produced by neodymium-doped yttrium aluminum garnet ($Nd : Y_3Al_5O_{12}$) crystals with a wavelength of 1064-nm. These detectors use test masses to detect the spacetime vibrations produced by gravitational waves. In order to reduce noise in the signals due to

tectonic and meteorologic effects, every component of the detector is mounted into a stage that isolates vibrations [1].

2.2.2. Very Long Baseline Interferometry (VLBI)

During 2019, the Event Horizon Telescope Collaboration (EHTC) presented the first observation of the shadow of a black hole [9]. The collaboration implemented a technique known as very long baseline interferometry (VLBI), which consists in separating each element of the detector by distances that do not allow for communication in real time between each of the elements. This technique is usually employed by using several telescopes or observatories, of common astrophysical use, associated by a correlation function, in order to recreate a more complete observation of the source. The data collected by each of these detectors is then sent to a central compound in order to reconstruct the full picture by studying each data set. [128]

In the case of the Event Horizon Telescope (EHT), the detectors are placed around the planet. Each of these detectors is a telescope that is able to observe in millimeter or sub-millimeter wavelength. The distribution and the wide range of wavelengths of the detectors allow for a more complete survey of the astrophysical environment and a sufficient quality in order to achieve the needed resolution to study near-horizon details.

An array such as the one described here, is characterized by several factors such as [7]:

- Angular resolution. It is a measure of the resolution of the observation, a higher value allows for smaller details to appear in the reconstructed image. The EHT shows an angular resolution of $38 \mu as$ in the observation of M87, in contrast with the resolutions of mas obtained with a typical VLBI array [128].
- Atmospheric transparency. The location of the telescopes involved in the array allows for a medium with sufficient transparency such that the observations are not affected by the atmosphere.
- Scattering and optically thin accretion disks. This factor is related to the sources, as the wavelengths in which the observations are made are sufficient enough as to distinguish the effects produced by near horizon effects from the scattering produced by free electrons.

The observations made in 2017 by the EHTC, employed an array of eight telescopes and it presented the first extension of VLBI of wavelengths up to 1.3 mm. The complete description about the array and instrumentation implemented by the EHTC is described in [7].

3. Numerical relativity and general relativistic magnetohydrodynamics

The analysis of the phenomena described in section 2 is usually done by employing either the covariant formalism, which allows for a geometric description of the problem, or with the use of computers, which receive a decomposed spacetime to analyze dynamical effects in order to have a more intuitive notion of the concept of time evolution. This is done by implementing a new formalism which consists in solving the equations from general relativity using numerical methods. In order to apply these algorithms and to study the temporal evolution, the spacetime must be separated into spatial and temporal components. One of the most important and commonly used approaches to this problem is known as the 3+1 formalism, briefly discussed in the next section.

The use of 3+1 decomposition allows for the study of more realistic problems, such as the accretion process, which is one of the main topics in this work. In order to study this problem in the context of general relativity, a new formalism must be introduced which needs to be consistent with the 3+1 formulation. After this new set of equations is presented, the numerical methods needed to implement this procedure in a working algorithm are discussed.

3.1. 3+1 formulation

The main goal of this formalism is to provide the means to establish Einstein's equations as a Cauchy problem in order to solve the system by specifying initial data and using numerical methods to study the evolution. A discussion of the Cauchy problem can be found in Appendix A.

The first step in order to implement this framework, is to define the concept of foliation as done by [45, 77], applying the concept to a spacetime such that it acquires physical meaning. Then a brief review of the constraints imposed by the spacetime physical structure is presented in order to finally construct the ADM evolution equations.

3.1.1. Foliations and hypersurfaces

Considering an n -dimensional manifold \mathcal{M} , a foliation consists in slicing the spacetime into hypersurfaces Σ_t with $(n-1)$ -dimensions which is directly related to an scalar, smooth field \hat{t} with non-vanishing gradient such that the corresponding hypersurfaces associated to different values evaluated for the field

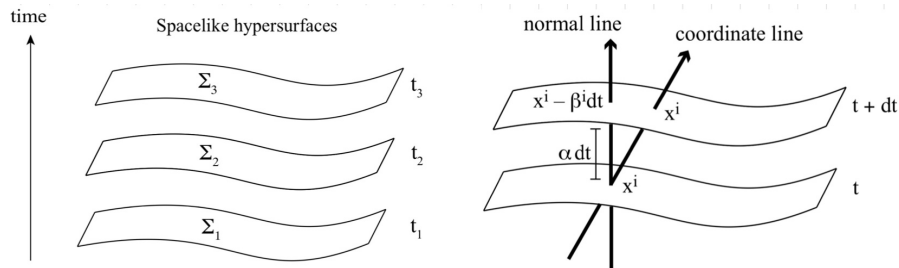


Figure 2: Spacetime foliations (Left.) representing space-like hypersurfaces associated to different values of the parameter t . (Right.) Adjacent hypersurfaces depicting the change in coordinates [77].

are non-intersecting:

$$\begin{aligned} \forall p \in \mathcal{M} \exists t \in \mathcal{R}, \text{ s.t. } \hat{t}(p) = t \\ \Sigma_t \cap \Sigma_{t'} = \emptyset \quad \forall t \neq t' \text{ s.t. } \mathcal{M} = \bigcup_{t \in \mathcal{R}} \Sigma_t \end{aligned} \quad (1)$$

A graphical representation of this foliations can be found in Figure 2 for the special case where the parameter t is associated with the time coordinate. Physical spacetimes may fulfill the definition given in eq. (1) as long as a Cauchy surface exists. This is due to the fact that these spacetimes are globally hyperbolic. Further discussion on this aspect is shown in Appendix A.

Information about the evolution of this slices can be found by analyzing adjacent hypersurfaces. Consider foliations corresponding to a parameter t and $t + dt$ as shown in Figure 2. The geometry associated to a generic spacetime can be determined by three factors, the three-dimensional metric, the lapse of proper time and the shift vector [77].

Although it must be noted that the physical properties of the original spacetime remain, its mathematical structure is going to adjust itself in order to be compatible with numerical simulations. When the original metric acts on the hypersurface it produces an induced metric, denoted by γ and known as three-dimensional metric, with elements given by γ_{ij} . It allows to establish the notion of length over every hypersurface.

In order to understand the role of the time lapse, consider a unitary vector \hat{n} , normal to a given slice Σ_t . This vector can be seen as the velocity from an observer moving in the temporal direction t (eulerian or fiducial observer), however, this observer perceives a proper time τ which is different to the coordinate time t . The lapse function α , acts as the ratio between the observer and the coordinate temporal rates along an Eulerian world line: $d\tau = \alpha dt$ [129]. It can

be noted that this same vector n , projects objects into the hypersurfaces, such that, for the specific case of the metric γ :

$$\gamma_{\mu\nu} = g_{\mu\nu} + n_\mu n_\nu \quad (2)$$

A vector \hat{t} can be defined which follows the flow of coordinate time world-lines, following the definition of the lapse function and the fact that any vector can be decomposed into the orthogonal and tangent projection:

$$t^\mu = \alpha n^\mu + \beta^\mu \quad (3)$$

Considering now the global time function t associated with a given foliation (not to be confused with the vector defined in eq. (3)), its gradient must be parallel to the orthogonal vector \hat{n} , i.e., they must be related by a proportionality constant which turns out to be α , then using eq. (3):

$$\hat{n} = -\alpha \nabla t \quad \rightarrow \quad \hat{t}^\mu \hat{n}_\nu = -\alpha \quad \rightarrow \quad \hat{t}^\mu \nabla_\mu t = 1 \quad \rightarrow \quad \beta_\mu = \gamma_{\mu\nu} \hat{t}^\nu \quad (4)$$

With the discussion above, the three parameters $\gamma_{\mu\nu}$, α and β_i , can be understood looking at a system such as the one shown in Figure 2. The three-dimensional metric can be understood in terms of a single foliation, as the geometry of such slice, while the lapse and the shift vector, are associated to the evolution for a given observer between adjacent slices, the first with the temporal length and the second with the displacement vector over the hypersurfaces.

The line element of a spacetime generated under the slicing conditions mentioned above is given as:

$$ds^2 = -(\alpha^2 - \beta_i \beta^i) dx^{02} + 2\beta_i dx^i dx^0 + \gamma_{ij} dx^i dx^j \quad (5)$$

In this coordinate system, the normal vector corresponding to the velocity measured by an eulerian observer is given by:

$$n_\mu = (-\alpha, 0), \quad n^\mu = (1/\alpha, -\beta^i/\alpha) \quad (6)$$

An important property appears when considering this system, as the relation between the determinants associated to the 4-dimensional metric and the spatial metric, is given then by:

$$\sqrt{-g} = \alpha \sqrt{\gamma}. \quad (7)$$

It is important to mention that as the slicing is done in an arbitrary, non-unique way, although α and β_i are introduced in a way such that they are coordinate independent, they take the role of gauge functions.

3.1.2. ADM/York evolution equations

In order to obtain the evolution equations for a generic gravitational problem, there are two approaches that can be followed in this formulation. The first one, the original ADM (Arnowitt-Deser-Misner) formulation [14], consists in a Lagrangian/Hamiltonian analysis starting from the gravitational action to obtain evolution equations for the three-dimensional metric γ_{ij} , and its canonical conjugate momentum π_{ij} . The second approach was proposed by York [135], consisting in the study of geometrical projections of the curvature tensors over the hypersurfaces. Although the physical meaning is the same for both approaches, they are not mathematically equivalent as their solutions only converge in a subset of the complete family of solutions. In this section, we focus on the York formulation following the treatment presented in [77].

As discussed before, the three-dimensional metric γ , represents the geometry of a given hypersurface, or equivalently, its curvature (by analyzing the curvature tensors). However, it does not provide information about how the geometry acts in the global level, i.e., how are the different slices affected by each other. To analyze this extrinsic curvature in the context of foliations, the normal vectors mentioned above are useful, as they can define a purely spatial symmetric curvature tensor such as:

$$K_{\mu\nu} = -\gamma_{\mu}^{\alpha}\nabla_{\alpha}n_{\nu} = -(\nabla_{\mu}n_{\nu} + n_{\mu}n^{\alpha}\nabla_{\alpha}n_{\nu}) \quad (8)$$

By employing the definition of the Lie derivative over γ along the normal direction:

$$\begin{aligned} \mathcal{L}_{\hat{n}}\gamma_{\mu\nu} &= n^{\alpha}\nabla_{\alpha}\gamma_{\mu\nu} + \gamma_{\mu\alpha}\nabla_{\nu}n^{\alpha} + \gamma_{\nu\alpha}\nabla_{\mu}n^{\alpha} \\ &= \gamma_{\mu}^{\alpha}\nabla_{\alpha}n_{\nu} + \gamma_{\nu}^{\alpha}\nabla_{\alpha}n_{\mu} = -2K_{\mu\nu} \end{aligned} \quad (9)$$

The fact that the curvature tensor can be expressed in terms of a Lie derivative implies that it can be seen as a velocity measured by the Eulerian observers moving along the world-lines defined by \hat{n} .

Due to the algebraic properties of the Lie derivative, and using eq. (3), the curvature tensor can be re-expressed as:

$$\begin{aligned} K_{\mu\nu} &= -\frac{1}{2\alpha}\mathcal{L}_{\alpha\hat{n}}\gamma_{\mu\nu} = -\frac{1}{2\alpha}\left(\mathcal{L}_{\hat{t}} - \mathcal{L}_{\hat{\beta}}\right)\gamma_{\mu\nu} \\ &\hookrightarrow \left(\partial_t - \mathcal{L}_{\hat{\beta}}\right)\gamma_{ij} = -2\alpha K_{ij} \end{aligned} \quad (10)$$

Eq. (10) represents the temporal evolution of the spatial metric, as the deduction of this equation does not involve the Einstein equations, the γ evolution does not have dynamical information.

In order to obtain information about the dynamics of the spacetime, Einstein equations must be expressed in 3+1 formulation, which can be done by projecting them into an hypersurface. Remembering that the Einstein equations are relations between the spacetime geometry and the content of matter present in it, a good way to start is to find the projections of the Riemann tensor, (which is done by applying the projector $\gamma_\beta^\alpha = \delta_\beta^\alpha + n^\alpha n_\beta$ over each component) as well as the contraction with the normal vector \hat{n} :

$$\begin{aligned}\gamma_\alpha^\delta \gamma_\beta^\kappa \gamma_\mu^\lambda \gamma_\nu^\sigma R_{\delta\kappa\lambda\sigma} &= {}^{(3)}R_{\alpha\beta\mu\nu} + K_{\alpha\mu} K_{\beta\nu} - K_{\alpha\nu} K_{\mu\beta} \\ \gamma_\alpha^\delta \gamma_\beta^\kappa \gamma_\mu^\lambda n^\nu R_{\delta\kappa\lambda\sigma} &= \gamma_\beta^\nu \nabla_\nu K_{\alpha\mu} - \gamma_\alpha^\nu \nabla_\nu K_{\beta\mu}\end{aligned}\quad (11)$$

This results in the Gauss-Codazzi and Codazzi-Mainardi equations respectively, which are discussed in great detail in the context of physics in [20, 81, 82], while a brief review of the fundamental mathematical formulation from these equations can be found in [68].

Following the procedure shown in [77], contracting and using the Einstein equations, the Gauss-Codazzi and Codazzi-Mainardi equations, respectively take the form:

$$\begin{aligned}{}^{(3)}R + K^2 - K_{ij}K^{ij} &= 16\pi\rho & \text{Energy constraint} & \rightarrow 1 \text{ eq.} \\ \gamma_i^k \nabla_k (K^{ji} - \gamma^{ji}K) &= 8\pi j^j & \text{Momentum constraints} & \rightarrow 3 \text{ eqs.}\end{aligned}\quad (12)$$

where, over a foliated system, $\rho = n^\mu n^\nu T_{\mu\nu}$ represents the energy density and $j^i = -\gamma^{i\mu} n^\nu T_{\mu\nu}$ corresponds to the momentum density, both measured by an Eulerian observer. As these equations do not involve time derivatives, they can be considered as constraints that must be fulfilled in each hypersurface, this means that from the variables needed to specify the system (γ_{ij}, K_{ij}) , 4 are already specified and subjected to the constraints given by eq. (12).

Contracting the Riemann tensor two times with the normal vector, we find the remaining components of the Riemann tensor (the others determined by the Gauss-Codazzi and Gauss-Mainardi equations):

$$\gamma_\mu^\delta \gamma_\nu^\kappa n^\lambda n^\sigma R_{\delta\lambda\kappa\sigma} = \mathcal{L}_{\hat{n}} K_{\mu\nu} + K_{\mu\lambda} K_\nu^\lambda + \frac{1}{\alpha} \gamma_\mu^\lambda \nabla_\lambda \gamma_\nu^\beta \nabla_\beta \alpha \quad (13)$$

Combining with the Gauss-Codazzi and the Einstein equations, the dynamical evolution of the curvature components is found to be:

$$\begin{aligned}(\partial_t - \mathcal{L}_{\hat{\beta}})K_{ij} &= -\gamma_i^k \nabla_k \gamma_j^m \nabla_m \alpha + \alpha \left[{}^{(3)}R_{ij} + K K_{ij} - 2K_{ik} K_j^k \right] \\ &+ 4\pi\alpha [\gamma_{ij}(S - \rho) - 2S_{ij}]\end{aligned}\quad (14)$$

where $S_{\mu\nu} = \gamma_{\mu}^{\alpha}\gamma_{\nu}^{\beta}T_{\alpha\beta}$ represents the spatial stress tensor in an Eulerian frame. These equations are considered as the starting point of numerical relativity.

York's formulation is obtained by expressing the Einstein equations in terms of the Ricci tensor and using the curvature tensor, while the ADM formulation consists in the decomposition of the Einstein tensor $G_{\mu\nu}$ and the use of the canonical momentum associated to the spatial metric. In order to obtain these equations, the Hilbert action is used, given by

$$\mathcal{S} = \int_{\mathcal{V}} d^4x R \sqrt{-g} \quad \text{with} \quad \mathcal{V} = \bigcup_{t=t_1}^{t_2} \Sigma_t, \quad (15)$$

and using the 3+1 decomposition for the metric and the Riemann tensor, such that

$$\mathcal{S} = \int_{t_1}^{t_2} dt \left(\int_{\Sigma_t} \sqrt{\gamma} d^3x \alpha [R + K_{ij}K^{ij} - K^2] \right) = \int_{t_1}^{t_2} dt \int_{\Sigma_t} d^3x L. \quad (16)$$

As the spatial metric γ is considered as a dynamical variable, and usually the curvature tensor K is a function of $\dot{\gamma}_{ij}$ (as seen in eq. (10)), then its canonically conjugate momentum is given as:

$$\pi^{ij} = \frac{\partial L}{\partial \dot{\gamma}_{ij}} = \sqrt{\gamma} (K \gamma^{ij} - K^{ij}) \quad (17)$$

A more complete treatment on this derivation is shown in [45].

In order to determine how to maintain the constraints along the evolution, there are two different approaches, the first one, consists in monitoring violations of the constraints, which are initialized with an initial data solution, during the evolution of the spatial metric and the other variable (curvature tensor or canonical momentum) and is known as free evolution. The second approach consists in solving the constraint equations at every time step, which in turn, solves for some of the variables needed, while the rest are evolved with the remaining evolution equations and is known as constrained evolution, however, this last approach is more expensive to solve numerically [77].

Although the success of the ADM formulation, it has proven to evolve instabilities during numerical simulations. Recent work aims to either reformulate the equations or to introduce another formalism. An example of such attempts is known as the Baumgarte-Shapiro-Shibata-Nakamura (BSSN) formulation,

which, besides allowing for more accurate long-time evolution simulations, consists in the further decomposition of the spatial metric in terms of a conformal transformation [122, 19]. This is currently the most used formalism.

So far we have not made any considerations regarding the content of matter present in the spacetime. The next section deals with this issue in the context of fluids. In particular, in the perfect fluid approximation, where the fluid's self gravity can be neglected. Doing this allows to characterize the system in terms of the conservation equations, which together with the equation of state, represent the complete framework needed to study more complex cases, such as gravitational collapse, accretion (which is the main topic of this work), and even the evolution of neutron stars.

3.2. General Relativistic Magnetohydrodynamics

General relativistic magnetohydrodynamics (GRMHD) consists in a framework combining the concepts and equations from magnetohydrodynamics, which consists in the study of fluids subjected to magnetic interactions, with the formalism from general relativity. Classical magnetohydrodynamics consists in a set of conservation equations associated to the evolution of the fluid properties. This is going to be reflected in the general relativistic generalization as no clear distinction between space and time exist, although it can be mediated using the 3+1 formulation discussed previously.

This section consists in a brief introduction of the GRMHD equations, which are re-expressed in a 3+1 conservative set of equations by following the Valencia formulation.

3.2.1. GRMHD equations

The study of GRMHD arises from the need to analyze systems that can be studied in the context of fluids, which is reflected in the matter contained in the universe. The information regarding the content of matter in a spacetime is contained in the stress-energy tensor. When considering a geometry with non-trivial content of matter, the tensor $T^{\mu\nu}$ contains all the information relevant to the fluid contained in the spacetime.

In order to start this analysis, it is necessary to define a reference frame for the study of the fluids. Usually in classical MHD, two approaches are considered. The first, known as Lagrangian frame, consists in following an specific region of the fluid, i.e., an observer co-moving with the fluid. The Eulerian reference frame consists in fixing a point in space and time, and analyzing the flow circulating through such point. The general relativistic generalizations are immediate for

the Lagrangian approach, however, the Eulerian case consists in an observer following world-lines which remain orthogonal to the temporal hypersurfaces, such as in the previous section. [12, 124]. The Lagrangian approach has been widely used in 1-D problems, as it reduces numerical diffusion [46], however, in order to maintain hyperbolicity, it must be studied with a tetrad formalism [49]; it was first used in [83] in the context of gravitational collapse. Despite this discussion, along this work, the Eulerian description is adopted.

The more general way to model an unmagnetized fluid, is to define an energy-stress tensor as [46]:

$$T^{\mu\nu} = \rho(1 + \varepsilon)u^\mu u^\nu + (p - \zeta\theta)h^{\mu\nu} - 2\eta\sigma^{\mu\nu} + q^\mu u^\nu + q^\nu u^\mu \quad (18)$$

As for the variables involved in eq. (18), ρ represents the rest-mass density, ε the specific energy density, u^μ the fluid velocity, p for the pressure and q^ν is the energy flux. The viscosity of the system is given in terms of ζ and η , which represent the bulk and shear viscosity respectively and $\theta = \nabla_\mu u^\mu$ is the fluid expansion. We also define the shear $\sigma^{\mu\nu}$ and the projection tensor $h^{\mu\nu}$:

$$h^{\mu\nu} = g^{\mu\nu} + u^\mu u^\nu, \quad (19)$$

which is highly similar or analogous to eq. (3) for the spatial metric.

However, the most simple case, where the effects associated to energy loss (such as viscosity, shear or heat), are neglected, is known as a perfect fluid and it is the most common model used to study accretion. In this case, the stress-energy tensor is expressed in terms of the enthalpy h , and is reduced to:

$$T^{\mu\nu} = \rho h u^\mu u^\nu + p g^{\mu\nu}, \quad \text{where} \quad h = 1 + \varepsilon + \frac{p}{\rho}. \quad (20)$$

On the other hand, when dealing with a fluids that can interact with magnetic fields, the total stress-energy tensor is the sum of two components, the first one, regarding the electromagnetic (EM) interaction, and the other, associated to the hydrodynamic effects from the content of matter, such as in eq. (20). By introducing the field tensor associated to EM as $F^{\mu\nu}$ and its dual $\mathcal{F}^{\mu\nu}$ in a reference frame associated to an Eulerian observer moving with velocity n , as:

$$F^{\mu\nu} = n^\mu E^\nu - n^\nu E^\mu - \varepsilon^{\mu\nu\lambda\delta} n_\lambda B_\delta, \quad \mathcal{F}^{\mu\nu} = \frac{1}{2} \varepsilon^{\mu\nu\lambda\delta} F_{\lambda\delta}, \quad (21)$$

with E and B representing the electric and magnetic field respectively, and ε as the anti-symmetric Levi-Civita tensor divided by the metric determinant.

It is possible to obtain a frame where every component of the electric field vanishes, this is known as the ideal MHD approximation. The magnetic field b , is then given by:

$$b^\mu = \mathcal{F}^{\mu\nu} n_\nu, \quad b^2 = b_\nu b^\nu. \quad (22)$$

With this, the EM tensor takes the form:

$$T_{EM}^{\mu\nu} = F^{\mu\lambda}F_{\lambda}^{\nu} - \frac{1}{4}g^{\mu\nu}F^{\lambda\delta}F_{\lambda\delta} = \left(u^{\mu}u^{\nu} + \frac{1}{2}g^{\mu\nu}\right)b^2 - b^{\mu}b^{\nu}, \quad (23)$$

and considering the matter tensor, given by eq. (20):

$$T_{GRMHD}^{\mu\nu} = T_{\text{Matter}}^{\mu\nu} + T_{EM}^{\mu\nu} = \rho h^* u^{\mu} u^{\nu} + p^* g^{\mu\nu} - b^{\mu} b^{\nu} \quad (24)$$

with $p^* = p + \frac{b^2}{2}$ and $h^* = h + \frac{b^2}{\rho}$

The new variables p^* and h^* , are thus modified by the influence of the magnetic field.

The necessary variables to work in a GRHD analysis are related by an equation of state and evolved through conservation equations regarding the divergence of the stress-energy tensor. The first set of equations are obtained directly from the Bianchi identities, resulting in the conservation of the tensor $T_{\mu\nu}$, while another equation is obtained from the divergence of the projection over the Eulerian velocity, resulting in a continuity equation.

When considering GRMHD, another set of equations is introduced in the form of the Maxwell equations, such that for GRMHD, we are left with the following set of conservation laws:

$$\textbf{Continuity equation:} \quad \nabla_{\mu}(\rho u^{\mu}) = 0, \quad (25)$$

$$\textbf{Energy-momentum conservation:} \quad \nabla_{\mu}(T^{\mu\nu}) = 0, \quad (26)$$

$$\textbf{Maxwell equations:} \quad \nabla_{\nu}(\mathcal{F}^{\mu\nu}) = 0, \quad (27)$$

$$\textbf{Equation of state:} \quad P = P(X, Y) \quad (28)$$

In order to numerically implement these equations, they must be expressed in 3+1 formulation, although other formulations have been explored which consider hypersurfaces with different causal structures [99].

Starting from eq. (25), using also the definition for the Lorentz factor W for an Eulerian observer with 3-velocity v^i , $W = (1 - v^2)^{1/2} = -n_{\mu}u^{\mu} = \alpha u^t$ and eq. (7), the continuity equation can be expressed in 3+1 formulation as:

$$\nabla_{\mu}(\rho u^{\nu}) = \frac{1}{\sqrt{-g}}\partial_{\nu}(\sqrt{-g}\rho u^{\nu}) = \partial_t(\sqrt{\gamma}\rho W) + \partial_i(\alpha\sqrt{\gamma}\rho W\bar{v}^i) = 0 \quad (29)$$

where the advection velocity \bar{v}^i is introduced and defined in terms of the Eulerian 3-velocity v^i (also known as the Valencia 3-velocity) or the fluid velocity u^i , as $\bar{v}^i = v^i - \beta^i/\alpha = u^i/W$.

The conservation of the stress-energy tensor equation can be further simplified by projecting over the hypersurface with the help of the spatial metric. Taking into account the fact that $\nabla_\nu g^{\mu\nu} = 0$ and the relation between the covariant derivative and the Christoffel symbols $\Gamma_{\beta\delta}^\alpha$, this results in:

$$\gamma_{i\nu}\nabla_\mu T^{\mu\nu} = \partial_t(\alpha\sqrt{\gamma}T_i^t) + \partial_j(\alpha\sqrt{\gamma}T_i^j) - \alpha\sqrt{\gamma}T^{\mu\nu}(\partial_\mu g_{\nu i} + \Gamma_{\mu\nu}^\sigma g_{\sigma i}) = 0 \quad (30)$$

A more useful form of these equations are obtained when contracting with a vector n^μ along the direction of the hypersurface and subtracting the continuity equation:

$$\begin{aligned} \nabla_\mu(-n_\nu T^{\mu\nu} - \rho u^\mu) + T^{\mu\nu}\nabla_\nu n_\mu &= \nabla_\mu(\alpha T^{0\nu} - \rho u^\mu) + T^{\mu\nu}\nabla_\nu n_\mu = 0 \\ \Leftrightarrow \partial_t(\alpha\sqrt{\gamma}(\rho u^t - \alpha T^{00})) + \partial_i(\alpha\sqrt{\gamma}(\rho u^i - \alpha T^{0i})) &= \alpha\sqrt{\gamma}T^{\mu\nu}\nabla_\nu n_\mu \end{aligned} \quad (31)$$

Eq. (31) represents an evolution equation with a source term. This source term, reflect the exchange of energy and momentum throughout spacetime.

In order to rewrite Maxwell equations, it is important to remember that the magnetic field B^μ is purely spatial, and that due to the anti-symmetric properties of the tensor $\mathcal{F}^{\mu\nu}$, there are no Christoffel symbols associated to the covariant derivative, such that eq. (27) in 3+1 takes the form:

$$\partial_t(\sqrt{\gamma}B^\mu) = \partial_i\left(\frac{\alpha\sqrt{\gamma}}{W}(u^\mu B^i - u^i B^\mu)\right) \quad (32)$$

$$\mu = 0 \quad \rightarrow \quad \partial_i(\sqrt{\gamma}B^i) = 0 \quad (33)$$

$$\mu \neq 0 \quad \rightarrow \quad \partial_t(\sqrt{\gamma}B^i) = \partial_j(\sqrt{\gamma}(\bar{v}^i B^j - \bar{v}^j B^i)) \quad (34)$$

Eq. (33) is known as the solenoidal or divergence constraint for the magnetic field, which is an analogy of the divergence condition from Maxwell equations that implies the non-existence of magnetic monopoles, numerically this constraint is special, as it must be implemented on its own. On the other hand, eq. (34) represents an induction equation, which results in the evolution of the magnetic field.

3.2.2. Valencia Formulation

The Valencia formulation [18, 13] consists in introducing a new set of dynamical variables, known as conserved variables, and expressing the conservation equations (eqs. (25-27)) as a first order, flux-conservative system. This is done in order to take advantage of the new system's hyperbolicity, which allows for the implementation of numerical techniques discussed in the following sections.

Due to the form of the previous equations (eqs. (29), (31) and (33-34)), it is convenient to define the new set of variables [13]:

$$\begin{aligned}
 D &= \rho W, & \tau &= \rho h^* W^2 - p^* - (\alpha b^0)^2 - D, & b^2 &= \frac{B^i B_i}{W^2} + (B^i v_i)^2 \\
 S_j &= \rho h^* W^2 v_j - \alpha b^0 b_j, & b^0 &= \frac{W B^i v_i}{\alpha}, & b^i &= \frac{B^i}{W} + W (B^j v_j) \bar{v}^i
 \end{aligned} \tag{35}$$

under these new variables, known as conserved variables, the system of equations defined before, takes the form:

$$\partial_t (\sqrt{\gamma} D) + \partial_i (\alpha \sqrt{\gamma} D \bar{v}^i) = 0 \tag{36}$$

$$\begin{aligned}
 \partial_t (\sqrt{\gamma} S_j) + \partial_i \left[\alpha \sqrt{\gamma} \left(S_j \bar{v}^j + p^* \delta_j^i - \frac{b_j B^i}{W} \right) \right] \\
 = \alpha \sqrt{\gamma} T^{\mu\nu} (\partial_\mu g_{\nu i} + \Gamma_{\mu\nu}^\sigma g_{\sigma i})
 \end{aligned} \tag{37}$$

$$\begin{aligned}
 \partial_t (\sqrt{\gamma} \tau) + \partial_i \left[\alpha \sqrt{\gamma} \left(\tau \bar{v}^i + p^* v^i - \alpha b^0 \frac{B^i}{W} \right) \right] \\
 = \alpha \sqrt{\gamma} (T^{\mu 0} \partial_\mu \ln \alpha - T^{\mu\nu} \Gamma_{\mu\nu}^0)
 \end{aligned} \tag{38}$$

$$\partial_t (\sqrt{\gamma} B^i) + \partial_k (\bar{v}^i B^j - \bar{v}^j B^i) = 0 \tag{39}$$

This choice of variables makes it possible for the system to be expressed as:

$$\frac{1}{\sqrt{-g}} \left[\frac{\partial \sqrt{\gamma} \mathbf{F}^0(\mathbf{w})}{\partial x^0} + \frac{\partial \sqrt{-g} \mathbf{F}^i(\mathbf{w})}{\partial x^i} \right] = \mathbf{s}(\mathbf{w}), \tag{40}$$

where \mathbf{w} represents the set of physical variables, which now are called primitive variables. \mathbf{F}^0 and \mathbf{F}^i represent the conserved fluxes, while \mathbf{s} is associated to the sources. These are given as:

$$\begin{aligned}
 \mathbf{F}^0(\mathbf{w}) &= \begin{pmatrix} D \\ S_j \\ \tau \\ B^k \end{pmatrix}, & \mathbf{F}^i(\mathbf{w}) &= \begin{pmatrix} D \bar{v}^i \\ S_j \bar{v}^j + p \delta_j^i - \frac{b_j B^i}{W} \\ \tau \bar{v}^i + p v^i - \alpha b^0 \frac{B^i}{W} \\ \bar{v}^i B^k - \bar{v}^k B^i \end{pmatrix}, \\
 \mathbf{s}(\mathbf{w}) &= T^{\mu\nu} \begin{pmatrix} 0 \\ \left(\frac{\partial g_{\nu j}}{\partial x^\mu} - \Gamma_{\nu\mu}^\delta g_{\delta j} \right) \\ \alpha \left(\delta_\nu^0 \frac{\partial \ln \alpha}{x^\mu} - \Gamma_{\nu\mu}^0 \right) \\ 0^k \end{pmatrix}
 \end{aligned} \tag{41}$$

Finally, in order to close the system, an equation of state must be introduced. This equation of state relates the primitive variables and from here, through derivatives between these relations, several physical parameters are obtained, an important quantity is the local sound velocity, denoted by c_s , and given by:

$$c_s^2 = \left(\frac{\partial p}{\partial e} \right)_s \quad (42)$$

Usually the solutions to GRMHD equations present discontinuities or shocks due to the non-linearity of the equations [98], however, by rewriting the conservation equations as a flux-conservative system, we guarantee that in such shock discontinuities, the Rankine-Hugoniot conditions are satisfied. This allows for the development of High resolution shock capturing methods (HRSC), and allow for the physical variables to be correctly modelled through the evolution.

3.2.3. Hyperbolic structure and Riemann problem

The following discussion follows mainly [13, 106], the reader is directed to these references for an extended treatment. These new equations fulfill the necessary conditions in order to be considered as hyperbolic (Appendix A). The fact that this approach only contains first derivatives, allows to obtain more information about the underlying structure of the equations by expressing them as a quasi-linear system, given by

$$\mathcal{A}_B^{\mu A} \nabla_\mu V^B = 0 \quad (43)$$

where V represents the set of physical variables, labeled by the indices A and B , which run through the k variables, while \mathcal{A} are the $k \times k$ jacobian matrices associated to the fluxes.

In the context of GRMHD, as was found in [13] (where more details about the construction of the jacobian matrices can be found), the variables associated, are given by $V = (u^\mu, b^\mu, p, s)$ where s represents the specific entropy. By obtaining the characteristic polynomial of this system, due to the structure of the equation, the eigenvalues can be found and interpreted as the speed of propagating waves. The complete procedure regarding this analysis for GRHD, as well as the interpretation of eigenvalues as waves, is available in more detail in chapter 4 of [106].

The characteristic equation for this configuration is given as

$$\mathcal{A}^\mu (\zeta_\mu - \lambda \xi_\mu) \mathbf{R} = \mathcal{A}^\mu \phi_\mu \mathbf{R} = 0 \quad (44)$$

where ζ and ξ represent an spacelike and a timelike vector respectively, i.e., they define a specific hypersurface. λ represents the eigenvalues and \mathbf{R} their associated eigenvectors.

Solving the system, results in 10 eigenvalues, however, two of them are eliminated by using the velocity invariants, which are considered as constraints, $u_\mu u^\mu = -1$ and $u_\mu b^\mu = 0$. Thus, the solution to this equation, considering propagation along the x -direction, is given by

$$\det(\mathcal{A}^\mu \phi_\mu) = (\rho h + b^2) a^2 \mathcal{A}^2 \mathcal{N}_4 = 0 \quad (45)$$

where

$$\begin{aligned} \mathcal{A} &= (\rho h + b^2) a^2 - \mathcal{B}^2, & a &= \frac{W}{a} (-\lambda + \alpha v^x - \beta^x), \\ \mathcal{N}_4 &= \rho h \left(\frac{1}{c_s^2} - 1 \right) a^4 - \left(\rho h + \frac{b^2}{c_s^2} \right) a^2 G + \mathcal{B}^2 G \\ \mathcal{B} &= b^x - b^0 \lambda, & G &= \frac{1}{\alpha^2} [-(\lambda + \beta^x)^2 + \alpha^2 \gamma^{xx}] \end{aligned} \quad (46)$$

The explicit dependence on the eigenvalues λ is encoded in the variable a , then from eq. (45), if $a = 0$, there is a wave, known as entropic wave, if $\mathcal{A} = 0$, two Alfven waves appear, while if $\mathcal{N}_4 = 0$, the solution reflects four magnetosonic waves, resulting in seven independent waves.

Entropic and Alfven solutions are given by

$$\lambda_e = \alpha v^i - \beta^i, \quad \lambda_{a\pm} = \frac{b^i \pm \sqrt{\rho h + B^2 u^i}}{b^0 \pm \sqrt{\rho h + B^2 u^0}} \quad (47)$$

while for magnetosonic waves, solutions cannot be expressed analytically due to the quartic character of the equation, but the waves can be separated into fast and slow, with two solutions for each speed. The velocity for each wave can be ordered in the following way:

$$\lambda_{f-} \leq \lambda_{a-} \leq \lambda_{s-} \leq \lambda_e \leq \lambda_{s+} \leq \lambda_{a+} \leq \lambda_{f+} \quad (48)$$

These solutions become relevant when trying to find the conserved fluxes from eq. (40), as the numerical solutions are given in terms of these speeds. They also play a fundamental role when determining the conditions necessary for implementing a time-step during dynamical evolution.

3.3. Numerical Methods

In order to obtain a solution for the system, the finite volume formulation is introduced. This allows for a suitable way to integrate the fluxes along a region by decomposing it into numerical cells that form part of a grid. Inferring the value of the fluxes along each cell and using the conservation equations, the system evolution is found. This section deals with the numerical methods needed in order to complete the procedure mentioned above by following the ideas from [106] and [46].

3.3.1. Finite volume formulation and High resolution shock capturing schemes

In order to obtain a discrete spatial domain, a 1-D spacetime is considered (as the 3D generalization is trivial in this case), J intervals are created in the form $I_j = [x_{j-1/2}, x_{j+1/2}]$. This interval represents a numerical cell of width $\Delta x = x_{j+1/2} - x_{j-1/2}$. The numerical time intervals are given by $[t^n, t^{n+1}]$, such that the cell volume is given by $V_j^n = I_j \times [t^n, t^{n+1}]$.

For a conservative and hyperbolic system without sources, of the form $\partial_t \mathbf{U} + \partial_x \mathbf{F} = 0$, integrating over the volume of a cell V_j^n , results in

$$\int_{x_{j-1/2}}^{x_{j+1/2}} dx U(x, t^{n+1}) = \int_{x_{j-1/2}}^{x_{j+1/2}} dx U(x, t^n) + \int_{t^n}^{t^{n+1}} dt F[U(x_{j-1/2}, t)] + \int_{t^n}^{t^{n+1}} dt F[U(x_{j+1/2}, t)] \quad (49)$$

In order to find a more suitable form for this equation (which is the differential equation in integral form), new variables are introduced:

$$\text{Cell Volume Average} \quad \mathbf{U}_j^n = \frac{1}{\Delta x} \int_{x_{j-1/2}}^{x_{j+1/2}} dx U(x, t^n) \quad (50)$$

$$\text{Numerical Flux} \quad \mathbf{F}_{j\pm 1/2} = \frac{1}{\Delta t} \int_{t^n}^{t^{n+1}} dt F[U(x_{j\pm 1/2}, t)] \quad (51)$$

such that eq. (49) takes the form:

$$\mathbf{U}_j^{n+1} = \mathbf{U}_j^n + \frac{\Delta t}{\Delta x} (\mathbf{F}_{j-1/2} - \mathbf{F}_{j+1/2}) \quad (52)$$

The numerical methods that employ this decomposition technique are known as finite volume methods. Due to the CFL condition, the fluxes should depend only on neighboring cells.

With these basic ideas, the problem from eq. (40), can be solved in the following way.

Considering a region Ω of the 4-D manifold, enclosed within an hypersurface which has spacelike and timelike boundaries given by Σ_t , $\Sigma_{t+\Delta t}$ and by Σ_{x^i} , $\Sigma_{x^i+\Delta x^i}$ respectively, defining the faces of a cell.

Defining the average over a cell as:

$$\bar{\mathbf{F}}^0 = \frac{\int_{x^1}^{x^1+\Delta x^1} \int_{x^2}^{x^2+\Delta x^2} \int_{x^3}^{x^3+\Delta x^3} \sqrt{\gamma} dx^1 dx^2 dx^3 \mathbf{F}^0}{\int_{x^1}^{x^1+\Delta x^1} \int_{x^2}^{x^2+\Delta x^2} \int_{x^3}^{x^3+\Delta x^3} \sqrt{\gamma} dx^1 dx^2 dx^3}, \quad (53)$$

Integration over Ω of eq. (40) yields:

$$\begin{aligned} \bar{\mathbf{F}}^0_{t+\Delta t} - \bar{\mathbf{F}}^0_t = & - \left(\int_{\Sigma_{x^1+\Delta x^1}} \sqrt{-g} dx^0 dx^2 dx^3 \hat{\mathbf{F}}^1 - \int_{\Sigma_{x^1}} \sqrt{-g} dx^0 dx^2 dx^3 \hat{\mathbf{F}}^1 \right) \\ & - \left(\int_{\Sigma_{x^2+\Delta x^2}} \sqrt{-g} dx^0 dx^1 dx^3 \hat{\mathbf{F}}^2 - \int_{\Sigma_{x^1}} \sqrt{-g} dx^0 dx^1 dx^3 \hat{\mathbf{F}}^2 \right) \\ & - \left(\int_{\Sigma_{x^3+\Delta x^3}} \sqrt{-g} dx^0 dx^1 dx^2 \hat{\mathbf{F}}^3 - \int_{\Sigma_{x^3}} \sqrt{-g} dx^0 dx^1 dx^2 \hat{\mathbf{F}}^3 \right) \\ & + \int_{\Omega} d\Omega \mathbf{S} \end{aligned} \quad (54)$$

Eq. (54) represents that the change in time of the flux averaged through a cell, is given in terms of the total fluxes calculated at the faces of said cell.

Remembering that, up to this point, the fluxes are given in terms of the conserved variables, we do not have information about the evolution of the physical variables. In order to recover the evolution of primitive variables from the set of eqs. (35), it is useful to construct a new system in terms of τ , S^2 and the definition of D . These, combined with eq. (40) form a new system of equations, from where the primitive variables can be recovered by finding the roots of such system.

The physical solution is continuous, not discrete, however, the solutions are given in the discrete regime, so that they must be reconstructed. In order to obtain this reconstruction, the fluxes must be calculated along each cell. This is usually done using HRSC methods, which consist in solving a local Riemann problem in every numerical cell.

A Riemann problem consists in an initial value problem where the initial conditions are given by constant and discontinuous values, physically analogous to the solution of a two-region system separated by a membrane. This solution is given in terms of a left and a right state [106]. As shown in figure 3, discontinuities can be found at the center of each numerical cell. This effect is associated to the discreteness of the solution and it is not physical, however, by solving a series of adjacent Riemann problems along the complete computational domain, it is possible to infer the physical solution. The constant value taken by

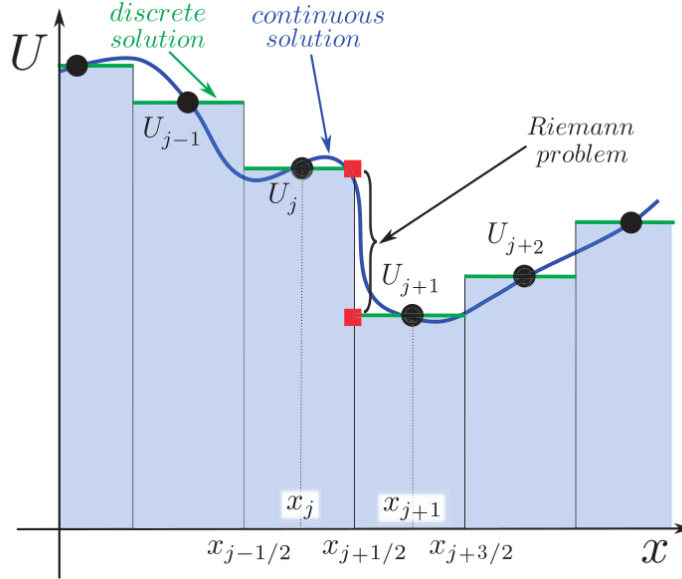


Figure 3: Riemann problem [106]

the discrete solution along a given cell is the average of the flux through such cell.

The steps to follow in order to solve a problem with HRSC methods are:

1. Reconstruct left/right states at each cell boundary through a Riemann problem.
2. Solve the Riemann problem (via exact or approximate Riemann solvers).
3. Evolve in time through a time-update algorithm.

A brief discussion of each step, as well as some of the main methods used, is contained in the following sections.

3.3.2. Reconstruction techniques

Usually the methods used to reconstruct the fluxes are variations from the original Godunov method, which is a first order accuracy scheme that consists

in using left/right states as:

$$U(x, t^n) = \begin{cases} U_j^n & x < x_{j+1/2} \\ U_{j+1}^n & x > x_{j+1/2} \end{cases} \quad (55)$$

Supposing the temporal evolution to be self-similar (i.e. the shape does not change, it is only re-scaled), the fluxes are easily calculated by combining eq. (55) with eqs. (50) and (51), such that:

$$U_j^{n+1} = \begin{cases} U_j^n - \lambda \frac{\Delta t}{\Delta x} (U_j^n - U_{j-1}^n) & \lambda > 0 \\ U_j^n - \lambda \frac{\Delta t}{\Delta x} (U_{j+1}^n - U_j^n) & \lambda < 0 \end{cases} \quad (56)$$

Modern Godunov methods aim to increase resolution in the calculation of the left/right states, usually they have at least 2nd order of accuracy (while the original method only worked up to 1st order) and a greater resolution in discontinuities.

The reconstruction process then consists in finding a suitable way to find the right and left states required by the Riemann problem from a given cell. For a cell centered at x_j , with its face located at $x_{j+1/2}$, the reconstruction phase consists in obtaining, for a set of integers k , $U_{j+1/2}^{L,R} = U_{j+1/2}^{L,R}(\{U_{j+k}\})$.

Two of the most used methods are known as the piecewise parabolic method [36], which consists in reconstructing the states via a polynomial interpolation with a parabola inside each cell, and the slope-limiter methods [132], which consists in a direct extension of the first order Godunov method by introducing a reformulation of eq. 56 and extrapolating in terms of a slope, several ways to express this slope have been studied.

3.3.3. Riemann solvers

Solving exactly the Riemann problem, is computationally expensive, thus approximate Riemann solvers, which although not being exact, work with a very high accuracy in most cases. These solvers can be subdivided into complete and incomplete depending on the number of waves that are considered in the solution. The discussion in this work is focused on approximate incomplete solvers due to the simplicity of their computational implementation. An extensive treatment of this subject is presented in [130].

One of the most commonly employed Riemann solvers is the Harten-Lax-Leer (HLL) solver, first shown in [55]. This solver assumes that after the discontinuity, only two waves are relevant. Each one of these, propagates in opposite directions, with speeds given by λ_R and λ_L respectively. For waves with speeds

between the latter, which represent the slower and the fastest possible speeds, the states are constant. This choice is represented in the fluxes as

$$F^{HLL} = \begin{cases} F_L & x/t < \lambda_L \\ \frac{\lambda_R F_L - \lambda_L F_R + \lambda_L \lambda_R (U_R - U_L)}{\lambda_R - \lambda_L} & \lambda_L < x/t < \lambda_R \\ F_R & \lambda_R < x/t \end{cases} \quad (57)$$

The wave speeds are computed via solving the eigenvalue problem in the form from eq. 47 and the criteria for choosing the bounds for these speeds is given by [40].

An special case for the HLL solver arises when considering $\lambda_R = -\lambda_L = \lambda$. This case is known as Rusanov solver or total variation diminishing Lax-Friedrichs flux. In this case, the fluxes are simplified to

$$F^{TVDLF} = \frac{1}{2}(F_L + F_R) - \frac{1}{2}\lambda(U_R - U_L) \quad (58)$$

This simplification has been applied to numerous problems providing good results. The Black Hole Accretion Code (BHAC), which is the code used in this work, employs both of this solvers.

3.3.4. Time update

One of the most common techniques in order to update the time period, is known as method of lines [114], as it is a standard procedure used in the context of numerical implementation of partial differential equations. It consists in transforming the current system into an ordinary differential equation in time that can be integrated. This is done by discretising the spatial part, while leaving the temporal derivative as a continuous function. This new system is now solved by using Euler step for first order accuracy and Runge-Kutta methods for higher order.

3.4. GRMHD codes

In order gain insight about the behaviour of accretion processes, it is necessary to solve the GRMHD equations for different spacetimes, however, doing this is complicated due to the numerous effects present in such processes. In order to do this, a number of numerical computational codes have been developed.

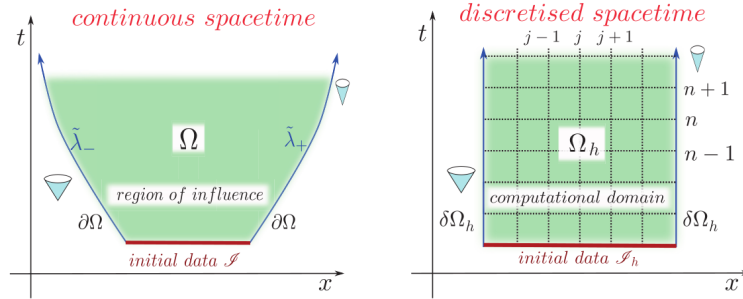


Figure 4: Schematic discretisation of an hyperbolic Cauchy problem [106]

3.4.1. Computational implementation of GRMHD equations

The numerical codes consist on an integration of the flux equations, which, in 3+1 formulation, take the form of an hyperbolic system of conservation laws [48], given by eq. (54).

In order to implement these equations (or any other Cauchy problem) in a numerical code, the spacetime must be discretised up to a certain resolution. This is done as discussed for the 3+1 formulation, however, in the computational domain, boundaries must be included. This is easier to understand graphically, as can be shown in figure 4. The process of discretisation, although it allows for numerical and computational methods to be implemented to solve the problem, it also generates numerical errors which can be divided into three categories as defined in [106]:

- Machine precision error. Associated to rational numbers expressed up to a finite figure.
- Round off error. Accumulation of machine precision errors when performing mathematical operations.
- Truncation error. Associated to the discretisation process.
 - Local truncation error. Measured by the difference obtained when applying the discretised operators to the exact solution.
 - Global truncation error. Spatial norm of the local truncation error.

The truncation errors are important as they allow to define the order of accuracy of the methods employed.

Convergence of the solution is also an important factor when dealing with discretised systems. In order to guarantee convergence, a consistency condition

is introduced which is fulfilled when the truncation error goes to zero in the continuum limit of the discretised problem [108]. The Lax equivalence theorem implies that stability is a sufficient and necessary condition for the convergence in these systems, as long as they fulfill the consistency condition. This stability condition, however, must be imposed, and is done by means of the Courant-Friedrichs-Lewy (CFL) condition, which ensures that the domain of the continuum problem is contained into the numerical domain. Physically, this condition implies that physical perturbations move through the domain slower than the numerical velocity defined as $\lambda_N = \Delta x / \Delta t$. The CFL constraint is usually given in terms of a dimensionless parameter $C_{CFL} \leq 1$. This is used in practice to constrain the timestep, which is done in order to ensure a stable evolution [38].

Returning to the problem of implementing the equations, specifically, regarding the constant t surfaces, if the variables follow a conservation equation from one boundary of the cell to the other, they remain conserved during the evolution as long as there is no interference from the computational domain or the sources. However, this is not the case for the magnetic field components, as they also need to fulfill the divergence constraint (given by eq. (33)), which is implemented manually.

There are two main methods to implement the divergence constraint, the first one, usually known as flux-interpolated constrained transport (FCT) [57] and the second one, known as constraint dampening or generalized lagrangian multiplier (GLM) [42].

The FCT method consists in keeping to zero (at machine precision) the sum of all the fluxes going through a specific cell, nullifying the divergence of the magnetic field. On the other hand, the GLM method, aims, as the name implies, to introduce a Lagrange multiplier associated to the divergence condition into the conservation laws. Divergence errors are transported to the boundaries at the speed of light, where it decays on a sufficiently small timescale, thus, removing divergences and recovering an hyperbolic system.

The approach from eq. (54), allows to obtain the conserved variables from \mathbf{F}^0 at each time step, however, in order to obtain the fluxes, the primitive variables are also needed. These variables are obtained by solving (or inverting) the equations for D , S_j and τ along with the use of the equations of state, however, no explicit solutions can be found due to the non-linearity of the algebraic system and thus, a numerical approach is required. [94]

Eq. (54) implies that all fluxes are calculated only at the edges of the cell. As these flows are not necessarily continuous, an HRSC scheme (High Resolution Shock capturing scheme, such as the ones discussed in section 3.1.2) is needed to solve the system. As mentioned before, this schemes consist on using Riemann solvers to compute the numerical fluxes between cells in order to capture possible discontinuities. A review of the available codes using HRSC schemes is given in

[47].

Most GRMHD codes use finite-difference schemes in order to obtain approximate solutions in a discretized space-time. The effectiveness of these schemes is measured by the difference between exact and numerical solutions, which is known as global error. As this error gets closer to zero, the convergence of the method increases. On the other hand, locally, numerical and exact solutions can also be compared, giving rise to the local or residual error, from which the order of accuracy can be computed, helping to determine the convergence order of the scheme. [46, 106]

Table 1 shows some of the HRSC codes used in GRMHD simulations, along with a brief description of their more relevant features (a more complete list can be found in [46]). Recently the EHT collaboration published a comparison of these codes, testing their viability to solve the evolution of magnetized accretion [102].

Code	Description
HARM [50]	HLL fluxes, constrained transport, 2D, however, 3d version available as harm-3d
BHAC [103]	Implements AMR (Adaptive Mesh Refinement) and MPI (Message Passing Interface), constrained transport and constrained dampening
Koral [110]	Includes radiation with an M1 closure scheme [76, 111], uses LF fluxes and FCT.
Athena ++ [125]	AMR and MeshBlocks, uses FCT
Gmunu [30]	LF, HLL and HLLE fluxes, instead of hyperbolic equations, uses elliptic solutions.

Table 1: Some GRMHD numerical codes

This work uses the BHAC (Black Hole Accretion Code), developed in 2017. It will be more thoroughly studied in section 6.2.

In order to obtain results which can verify the data provided by observations from the theoretical point of view, the validity of the GRMHD approximations implemented in the numerical codes must be analyzed, so that these are valid in the experimental context (such as the EHT).

In the context of accretion, the relevant problem is that of a magnetized torus (the description of which can be found in section 5.2). A comparison of GRMHD codes performance regarding this specific problem can be found in [102].

Magnetized accretion GMHRD codes consider ideal GRMHD (with the exception of Koral), this approximation includes the treatment of the accretion plasma as a fluid. The sources that exist in the EHT regime, such as Sagi-

tarius A and M87, both are low-luminosity active galactic nuclei [80, 71] and thus the accretion rate is low enough such that the flow forms an optically thin and geometrically thick disk. This results in a collisionless plasma due to the virial temperature, also known as radiatively inefficient accretion flow (RIAF). The collisionless plasma contributions are small compared to its deviation from a fluid in this case, thus allowing for an ideal GRMHD approximation to be accurate in this regime [102, 28].

3.4.2. Black Hole Accretion Code (BHAC)

As shown in Table 1, the Black Hole Accretion code (BHAC) uses the framework MPI-AMRVAC as one of its main features. [35] This framework is written in Fortran 90 and is originally aimed at solving hyperbolic partial differential equations with emphasis in shock related problems and conservation laws, although it recently has been enabled to solve elliptic PDEs [69]. It exploits parallel computing by using MPI (Message Passing Interface) in order to exchange information between computer nodes.

On the other hand, the adaptive mesh refinement method consists in adjusting the accuracy in highly sensitive regions in order to obtain greater precision and resolution. It is commonly employed in the analysis of hydrodynamics numerical problems where turbulence is present. This provides well defined grid boundaries and a simple data structure which is specially helpful to avoid unnecessary interpolations, thus, decreasing the computational costs. In the current case, AMR is needed in order to simultaneously solve the dynamics for small and large scales and to analyze the behaviour of the MRI instability.

BHAC employs the 3+1 spacetime decomposition technique and allows for different Riemann solvers, such as the standard HLL and TVDLF, and a modified TVDLF solver, which was first described in [62] and applied to GRMHD in [105].

The code allows for the implementation of different equations of state (EOS) as long as the enthalpy can be analytically expressed in terms of density and pressure. Currently, models for ideal gas, synge gas and isentropic flow equations of state are implemented. Regarding the divergence constraint, BHAC employs both GLM and FCT in order to clean divergences.

One of the main advantages of BHAC is the flexibility that it provides regarding the addition of arbitrary spacetimes and coordinates. This is reflected in the fact that numerical metrics can be implemented besides the commonly known spacetimes. Currently, the code allows for the well known cartesian, Boyer-Lindquist, Kerr-Schild systems, as well as for less known systems, such as modified Kerr-Schild [85], Hartle-Thorne [56] or Rezolla & Zhidenko parametrization [107].

The documentation, the installation process and some tutorials for BHAC can be found in <https://bhac.science/>, as the code is publicly available.

4. Compact objects

Compact objects represent excellent tests of the strong regime of gravity due to the extreme conditions in their vicinity which give rise to interesting and unusual effects. The study of such effects by modern experiments has opened a new age in gravitational physics. This section deals with the basic physical properties of some of these objects, starting with the well-studied Schwarzschild black hole, up to the novel Proca stars, as well as addressing some of their shared features.

4.1. The physics of black holes and compact objects

In order for a massive object to be considered as compact, the necessary condition is given by $M/R \gg 1$, meaning that there is a great amount of mass contained into a small radius. Some objects that are considered as compact are neutron stars and black holes. However, extended theories of gravity allow for some other objects of exotic nature to be considered along this criteria. These stellar structures can (and should) be studied from different perspectives, as they contain a rich combination of physics from different scales, from particle and nuclear physics, up to gravitation and astrophysics.

There is a fundamental difference between a compact star and a black hole, the latter presents an event horizon which acts as a boundary that causally disconnects the inner region from the outside. This horizon is, in most cases, enough to find observable differences when observing (directly or indirectly) a compact object, however, there are some special cases when stars can produce an apparent horizon due to hydro-dynamical effects produced by matter that orbits around the center of gravity.

Black holes can be classified in terms of their mass. Primordial black holes usually are found in the early universe with masses up to that of the Sun, however, up to now, their formation channels are not determined. The next class of black holes are known as stellar, with masses between $2 - 50 M_{\odot}$, they are usually formed by gravitational collapse of massive stars. Next, are intermediate mass black holes, ranging from $50 - 10^5 M_{\odot}$ although it is not clear if these objects can be formed. High-redshift black holes, with masses between $10^5 - 10^6 M_{\odot}$, formed by collisions from super massive clouds. The final kind of black holes that can be found, are known as supermassive black holes with higher masses than $10^6 M_{\odot}$, they can be found in the center of most galaxies [26].

For isolated, generic, non-rotating stars, the spacetime can be modelled in terms of two regions. The inner region contains the material, which can be understood as a fluid associated with the solution of Einstein equations regarding the content of matter and the outer region, which usually represents an asymp-

totically flat spacetime. The line element associated to these objects is given, in Schwarzschild coordinates, as [97]:

$$ds^2 = -e^{\Phi(r)} dt^2 + e^{\lambda(r)} dr^2 + r^2 d\Omega^2 \quad (59)$$

And their structure is determined by the Tolman-Oppenheimer-Volkoff (TOV) equation, which constrains the pressure $P(r)$ and the total mass (in terms of the mass-energy density $\rho(r)$) as:

$$\frac{dP(r)}{dr} = -\frac{GM(r)\rho(r)}{r^2} \left(1 + \frac{P(r)}{\rho(r)c^2}\right) \left(1 + \frac{4\pi r^3 P(r)}{M(r)c^2}\right) \left(1 - \frac{2GM(r)}{c^2 r}\right)^{-1} \quad (60)$$

The parameters associated to the fluid, such as the pressure and density, are usually found in terms of the stress-energy tensor and can be obtained a more fundamental way, through the action. The total mass of the star is obtained through

$$M(r) = \int d^3x \sqrt{-g} (2T_0^0 - T_\mu^\mu) = 4\pi \int dr r^2 \rho. \quad (61)$$

When considering an arbitrary star, there is a critical mass at which further gravitational collapse into a black hole is inevitable. For white dwarfs, for example, this mass is known as the Chandrasekhar mass [29] and can be obtained in terms of an equation of state for a relativistic Fermi gas formed by massive particles. For a general fermionic star, this mass shows the limiting case when the gravitational pull surpasses the degeneracy pressure produced by its constituent particles, although for some stars, another forces can appear due to the interactions (For neutron stars, for example, neutrons are affected by strong nuclear force).

4.2. Schwarzschild Black Holes

This was the first solution to Einstein equations; it considers an static and isotropic metric that can describe the exterior region of a compact object, although it can be extended to other regions by means of coordinate transformations [134]. This solution, for an object with mass M , is given by

$$ds^2 = -\left(1 - \frac{2GM}{c^2 r}\right) c^2 dt^2 + \left(1 - \frac{2GM}{c^2 r}\right)^{-1} dr^2 + r^2 d\Omega^2 \quad (62)$$

This solution is asymptotically flat due to the fact that when $r \rightarrow 0$, eq. (62) is equivalent to a Minkowskian spacetime.

There is also a clear divergence when $r = r_S = 2GM/c^2$, which is known as the Schwarzschild radius. For objects where the surface is enclosed within this radius, a black hole appears.

This solution is not only important when working with black holes, but also when studying compact stars, when solving for the external region, i.e., a region with only empty space, due to Birkhoff's theorem, the only solution that fulfills the asymptotically flat condition is Schwarzschild metric [88].

The Schwarzschild solution is singular at two points, at $r = r_S$ and $r = 0$. A singularity can be produced by the coordinates or can be inherent to the geometry of spacetime. In order to determine the nature of the singularities present in this solution, it is necessary to observe the behaviour of the coordinate invariant quantities, for example, the contraction of the Riemann tensor

$$R_{\alpha\beta\mu\nu}R^{\alpha\beta\mu\nu} \sim \frac{1}{r^6}, \quad (63)$$

which presents the origin singularity, which can be regarded as an intrinsic singularity. However, the singularity associated to the Schwarzschild radius is not present. This indicates that the latter is an effect of the choice of coordinates and thus, can be removed by a suitable choice of coordinates.

Schwarzschild solution can be extended by employing Eddington-Finkelstein coordinates which consists in defining $v = t + r$ and $u = t - r$. The choice of either v or u allows to gain insight about the inner regions which correspond to a black hole and a white hole respectively. On the other hand, the maximal analytic extension of this spacetime is obtained when using the Kruskal-Szekeres coordinates, where $U = -e^{-\frac{u}{4M}}$ and $V = e^{\frac{v}{4M}}$. However, the new regions that can be formed by this extensions are not present in astrophysical black holes.

A Schwarzschild black hole can also cast a shadow, which is given by the the outermost orbit associated to null geodesics. The outer rim of this shadow is defined, for an observer, by the critical impact parameter associated to photons. For Schwarzschild metric, this is given by $b_{ph} = 3\sqrt{3}\frac{GM}{c^2}$. A detailed derivation for this value is found in [61]. However, in a realistic astrophysical situation, an accretion disk is present which deforms the photon ring and creates background radiation although the size of the shadow is barely affected [92].

Schwarzschild black hole is the simplest black hole that can be found, as it only depends on one parameter, the mass. Black holes, however, can present other features, such as rotation. Rotating black holes are known as Kerr black holes, and are described, in Boyer-Lindquist coordinates, by the following line element:

$$ds^2 = - \left(1 - \frac{2mr}{\Sigma} \right) dt^2 - 4mra \frac{\sin^2 \theta}{\Sigma} dt d\phi + \frac{\Sigma}{\Delta} dr^2 + \Sigma d\theta^2 + \left(r^2 + a^2 + \frac{2mra^2 \sin^2 \theta}{\Sigma} \right) \sin^2 \theta d\phi^2 \quad (64)$$

$$\text{with } \Sigma = r^2 + a^2 \cos^2 \theta, \quad \Delta = r^2 + a^2 - 2mr \quad \text{and} \quad a = \frac{J}{M}.$$

4.3. Boson stars

A boson star can be defined as a compact, regular object produced by the gravitational collapse of clouds composed of bosonic particles with a sufficient mass such that the gravitational collapse stops before becoming a black hole. These particles have integer spin and follow the Bose-Einstein statistics. Their formation channels have been studied in [119], where usually these stars could be formed through collision or accumulation of these bosonic particles, however, in order for an stable configuration to be achieved, the exceeding material must be radiated away, and this is done through gravitational cooling.

Fermionic stars (such as neutron stars and white dwarfs) are supported against gravity due to a degeneracy pressure associated to the fact that fermions cannot occupy the same energy level, a phenomenon that is not present in boson stars, thus stability is an important factor when studying boson stars [58]. Unstable boson stars can experience further collapse and transform into a black hole or the bosonic particles can be dispersed into the interstellar medium, although there is a possibility that the boson star can migrate into an stable solution [118].

Regular time-independent solutions are, in principle, forbidden by a theorem established by Derrick, however, in order for them to exist, an harmonic time dependence can be established, resulting in temporal oscillations of a complex scalar field [11]:

$$\Phi(\mathbf{r}, t) = e^{-i\omega t} \phi(\mathbf{r}) \quad (65)$$

Boson stars then can be explained as a massive complex scalar field which is minimally coupled with gravity through the action [115]:

$$\mathcal{S} = \int \frac{dx^4 \sqrt{-g}}{16\pi G} [R + 8\pi G (g^{\mu\nu} \partial_\mu \Phi^* \partial_\nu \Phi - V(|\Phi|^2))] \quad (66)$$

Due to the fact that boson stars emerge naturally when coupling a scalar field with gravity, they represent a prediction that comes directly from general relativity.

The interaction potential $V(|\Phi|^2)$ is important as it allows for different critical masses to appear due to the self-interaction terms. This potential can also contain information about stability and properties such as charge and rotation. Variation of this action results in a system composed by Einstein equations, with an stress-energy tensor given by

$$T_{\mu\nu}(\Phi) = \frac{1}{2} [\partial_\mu \Phi^* \partial_\nu \Phi + \partial_\mu \Phi \partial_\nu \Phi^*] - \frac{g_{\mu\nu}}{\sqrt{-g}} \mathcal{L}(\Phi), \quad (67)$$

and a Klein-Gordon equation governing the scalar fields:

$$\left(\square + \frac{dV(|\Phi|^2)}{d|\Phi|^2} \right) \Phi = 0. \quad (68)$$

This system, composed by Einstein and Klein-Gordon equations, is known as Einstein-Klein-Gordon equations. It is also interesting to note that the solutions are time-independent due to the fact that only the amplitude of the scalar field is considered in the potential. For a real scalar field solution, time dependence could appear resulting in a time-dependent metric solution.

The solution to this equations for an static, spherically symmetric metric, is given by:

$$ds^2 = -N(r)\sigma^2(r)dt^2 + \frac{dr^2}{N(r)} + r^2(d\theta^2 + \sin^2\theta d\phi^2) \quad (69)$$

It is important to note that although this metric is stationary due to the fact that the equations only consider the amplitude of the field, this scalar field associated to matter and the spacetime metric do not share the same symmetries.

The critical mass estimation for boson stars to be stable [64] shows that this parameter is given by $M_{max} = 0.633 M_{Pl}^2/m$, however, when considering a potential terms of higher order (such as λ^4), the available masses for boson stars increase dramatically.

Establishing a similar system to the TOV equations from eq. (60) accompanied by the Klein-Gordon equation, there are three equations that govern the evolution of this system. Supposing a potential of the form $V = -\mu^2|\Phi|^2$, these are given as:

$$\begin{aligned} m'(r) &= 4\pi r^2 \left(N(r)\phi'^2(r) + \mu^2\phi^2(r) + \frac{\omega^2\phi^2(r)}{N(r)\sigma^2(r)} \right) \\ \sigma'(r) &= 8\pi\sigma(r)r \left(\phi'^2(r) + \frac{\omega^2\phi^2(r)}{N^2(r)\sigma^2(r)} \right) \\ \phi''(r) + \frac{2\phi'(r)}{r} + \frac{N'(r)\phi'(r)}{N(r)} + \frac{\sigma'(r)\phi'(r)}{\sigma(r)} - \frac{\mu^2\phi(r)}{N(r)} + \frac{\omega^2\phi(r)}{N^2(r)\sigma^2(r)} &= 0 \end{aligned} \quad (70)$$

These equations are integrated with suitable initial conditions in order to explore other features such as their stability and evolution.

It is possible to generalize this results for a rotating boson star [136], where the ansatz for the scalar field now takes the form

$$\Phi(t, r, \theta, \phi) = \phi(r)Y_{lm}(\theta, \phi)e^{-i\omega t} \quad (71)$$

The appearance of the spherical harmonics in the scalar field description, produces different topologies for the boson stars, this can be related to the fact

that simulations of spinning boson stars evolution result in instabilities most of the time as shown in [112].

4.4. Proca Stars

Proca stars, as their scalar equivalents, are represented by regular and asymptotically flat geometries, with the difference that they are formed by a vector field of spin-1. Their mechanisms of formation are similar to that of boson stars, clouds containing these massive vectorial particles collide and the material starts clustering into the star up to the critical mass. The exceeding material is radiated away through gravitational cooling [44]. When the star is formed, it can either remain or turn to a stable state, it can collapse or it can even get dispersed through the interstellar medium.

For spherically symmetric Proca stars, the line element in the most general form is given in the same form as eq. (69). The Proca field is described by a complex 1-form given by the potential \mathcal{A} . The exterior derivative results in the field strength tensor $\mathcal{F} = d\mathcal{A}$, such that by coupling this field to gravity and without considering self-interactions, the action takes the form:

$$\mathcal{S}^{Proca} = \int d^4x \sqrt{-g} \left(\frac{R}{16\pi G} - \frac{1}{4} \mathcal{F}_{\alpha\beta} \bar{\mathcal{F}}^{\alpha\beta} - \frac{1}{2} \mu^2 \mathcal{A}_\alpha \hat{\mathcal{A}}^\alpha \right) \quad (72)$$

A dynamical condition which appears when studying this action is the Lorentz condition, given by $\nabla_\alpha \mathcal{A}^\alpha = 0$, which stops being an optional choice of gauge.

As for the explicit form of the potential, the same ansatz as in the boson star case is applied (however, instead of a scalar, a 1-form) in terms of an harmonic dependence.

$$\mathcal{A} = [f(r)dt + ig(r)dr] e^{-i\omega t} \quad (73)$$

This system is then determined through the Einstein equations and the Proca equations:

$$\begin{aligned} G_{\alpha\beta} &= 8\pi G T_{\alpha\beta} \\ \nabla_\alpha \mathcal{F}^{\alpha\beta} &= \mu^2 \mathcal{A}^\beta \end{aligned} \quad (74)$$

The energy momentum tensor associated to this action has the following form:

$$T_{\alpha\beta} = -\mathcal{F}_{\sigma(\alpha} \bar{\mathcal{F}}_{\beta)}^{\sigma} - \frac{1}{4} g_{\alpha\beta} \mathcal{F}_{\sigma\tau} \mathcal{F}^{\sigma\tau} + \mu^2 \left[\mathcal{A}_{(\alpha} \bar{\mathcal{A}}_{\beta)} - \frac{1}{2} g_{\alpha\beta} \mathcal{A}_\sigma \bar{\mathcal{A}}^\sigma \right] \quad (75)$$

From the two Proca equations (for t and r),

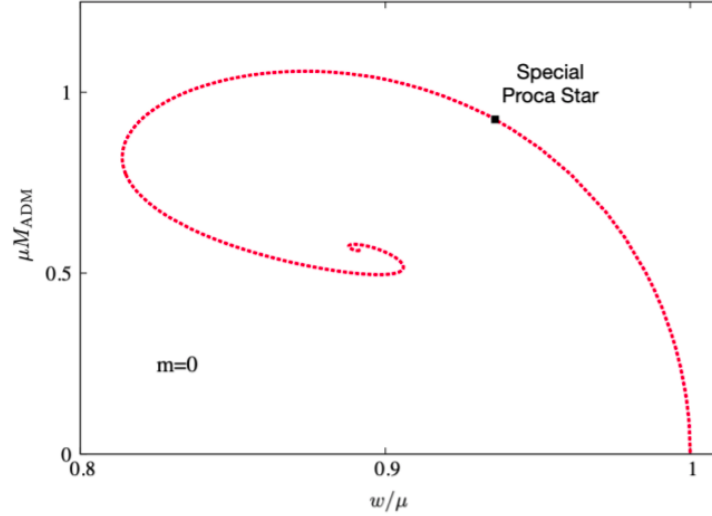


Figure 5: Parameter space of the Proca star solution [23].

$$\begin{aligned} \frac{d}{dr} \left[\frac{r^2(f'(r) - \omega g(r))}{\sigma(r)} \right] &= \frac{\mu^2 r^2 f(r)}{\sigma(r)N(r)} \\ \omega g(r) - f'(r) &= \frac{\mu^2 \sigma^2(r)N(r)g(r)}{\omega} \end{aligned} \quad (76)$$

On the other, hand, from Einstein equations:

$$\begin{aligned} m'(r) &= 4\pi Gr^2 \left[\frac{(f'(r) - \omega g(r))^2}{2\sigma^2(r)} + \frac{1}{2}\mu^2 \left(g^2(r)N(r) + \frac{f^2(r)}{N(r)\sigma^2(r)} \right) \right] \\ \frac{\sigma'(r)}{\sigma(r)} &= 4\pi Gr\mu^2 \left(g^2(r) + \frac{f^2(r)}{N(r)\sigma^2(r)} \right) \end{aligned} \quad (77)$$

The possible space of solutions given in terms of the parameters ω and μ are shown in figure 5. Reducing the frequency of the field produces an increase in the compactness of the solution up to a maximum value of $\omega_{max} = 0.875$. Several branches appear and the solutions continue spiraling through these different branches up to a critical frequency. The only stable branch is the one that connects $\omega = 1$ with ω_{max} . Every solution that appears in branches beyond this one develop instabilities [23] and eventually, it will either collapse into a black hole or gain enough mass such that it returns to the stable branch.

Spherically symmetric Proca stars usually have maximum stable masses of around $M_{Max} \simeq 1.058M_{Pl}^2/\mu$. This value is increased when considering spinning stars with respect to different integers of the harmonic index m [23]. In rotating

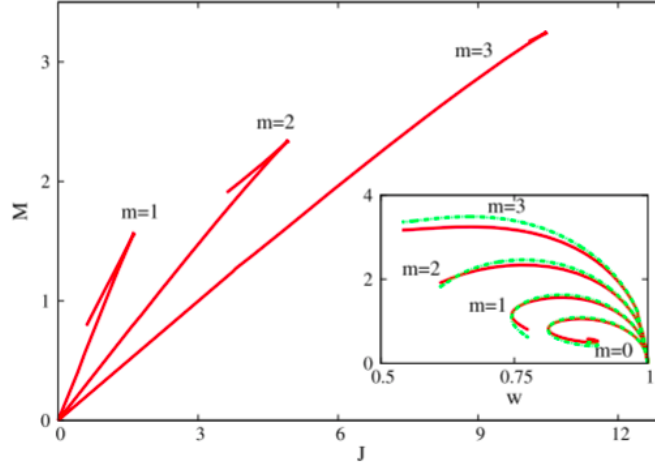


Figure 6: Solution curves associated to values of m [23].

Proca stars, the line element changes into

$$\begin{aligned}
 ds^2 = & -e^{2F_0(r,\theta)} dt^2 + e^{2F_1(r,\theta)} (dr^2 + r^2 d\theta^2) \\
 & + e^{2F_2(r,\theta)} r^2 \sin^2 \theta \left(d\phi - \frac{W(r,\theta)}{r} dt \right)^2, \quad (78)
 \end{aligned}$$

while the potential 1-form takes two extra functions in comparison with the spherically symmetric case,

$$\mathcal{A} = \left(\frac{H_1(r,\theta)}{r} dr + H_2(r,\theta) d\theta + iH_3(r,\theta) \sin \theta d\phi + iV(r,\theta) dt \right) e^{i(m\phi - \omega t)} \quad (79)$$

Different values of m account for an integer harmonic index, each generates a set of solution curves (the solution curve presented in figure 5 represents the case $m = 0$). Figure 6 shows the relation between the total mass and the angular momentum associated to the star, while the inset shows the equivalent to the spherically symmetric case for different values of m .

As mentioned before, when increasing the harmonic index, the maximum mass also increases and therefore, the associated frequency decreases. Another important property of these bosonic stars, is that the parameter $a = J/M$ is not constrained to be < 1 as in the Kerr case, resulting in a bigger family of solutions.

The stability of Proca solutions is studied in [113, 112]. For rotating boson stars, anomalous structures emerge due to the influence of spherical harmonics,

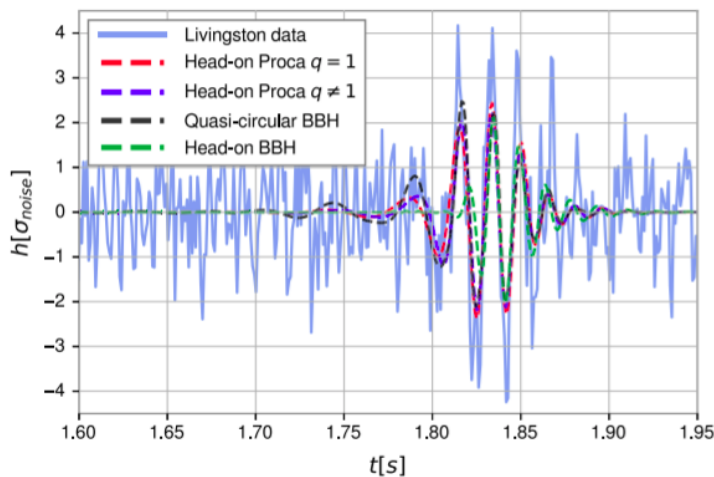


Figure 7: Time series and waveforms fitting the strain data of GW190521 [25].

while for Proca stars, the spheroidal nature prevails in every case. According to some authors, the anomalous structures in the case of boson stars could be responsible for the unstable evolution present in such objects [43].

4.5. Boson and Proca stars as black hole mimickers

In real astrophysical environments, Proca stars (and in general, boson stars or other compact objects) can act as black hole mimickers by reproducing effects that are only thought to be visible in black holes. This section presents a brief review of some of these effects, with specific focus on gravitational wave detection, shadows and simulations.

The observation by the LIGO-VIRGO collaboration of the event GW190521 [2] showed a final black hole merger with a total mass of $M \sim 142 M_{\odot}$. This is the range of masses associated to intermediate black holes, which, as discussed in section 4.1, have not been found up to this time. This fact raises questions about the nature of the compact objects involved in this process. The inspiral phase associated to this event falls out of the detector’s sensitivity, thus allowing for other options to be explored instead of binary mergers, such as head-on collisions of compact objects.

By means of Bayesian parameter estimation, the event GW190521 has been compared with numerical simulations regarding different configurations of Proca stars [25], showing a slightly preferred likelihood for the Proca models.

Figure 7 shows the strain data associated to the observation by the LIGO-

Livingston detector along with two simulations of head-on collisions between Proca stars (one where both stars have the same mass), the binary black hole merger originally reported and a head-on collision from black holes. The model which adjusts better to this data is the unequal mass Proca collision simulation, closely followed by the equal mass model, being both slightly preferred to the models of binary black holes.

Another important fact regarding this work [25], is that the mass corresponding to the boson particle associated to Proca stars was found to be of around $8.7 \times 10^{-13} eV$, which is contained into the mass boundaries of ultra-light dark matter. Although a slight preference is shown towards Proca stars, future observations of gravitational waves in these same regimes of mass are needed in order to confirm or discard the possibility that Proca stars exist.

On the other hand, studies suggest that boson and Proca stars can also produce surfaces that can be confused with shadows. But first, it is important to note that apparent shadows from compact horizon-less objects can be produced either by theoretical degeneracy in the photon ring calculations or by environmental or astrophysical effects.

Theoretical degeneracy regarding the shadow of a black hole occurs when different geometries produce the same critical impact parameter for null geodesics without these geometries being isometric between them. The work presented in [66] establishes the different conditions and configurations needed for this degeneracy to occur:

For spherically symmetric configurations given in the generic form

$$ds^2 = -V(r)A(r)dt^2 + \frac{dr^2}{B(r)V(r)} + r^2d\Omega^2, \quad (80)$$

to be Schwarzschild-degenerate, there are two conditions that must be met. The first condition is that the angle of observation must be the same in both cases with respect to the observer, and the second condition implies that the impact parameter λ associated to the shadow, must be given as

$$\lambda = \frac{\sqrt{27}M}{\sqrt{A(r_{obs})}}. \quad (81)$$

where r_{obs} represents the radius associated to the observer position.

On the other hand, for generic stationary spacetimes to be Kerr-degenerate, the line element must have the following form:

$$ds^2 = -\frac{(\Delta - a^2 \sin^2 \theta)\bar{\Sigma}}{\Sigma^2} dt^2 + \frac{\bar{\Sigma}}{A_4 \Delta} dr^2 + \hat{\Sigma} d\theta^2 - \frac{4amr \sin^2 \theta}{\Sigma^2} \hat{\Sigma} d\phi dt + \frac{[(r^2 + a^2)^2 - a^2 \Delta \sin^2 \theta] \hat{\Sigma}}{\Sigma^2} \sin^2 \theta d\phi^2 \quad (82)$$

where Δ and Σ are defined in the same way as for the Kerr spacetime in eq. (64), and $\hat{\Sigma} = r^2 A_1 + a^2 \cos^2 \theta B_1$. The functions A_1 , B_1 and A_4 , are free functions that must only fulfill the asymptotic flatness conditions.

An analysis of the stability of ultra compact objects that produce light rings, shows that horizon-less objects must present at least two light rings with one of them being stable, however, under short timescales, these objects could present instabilities making them unable to naturally mimic a BH [39].

Work has been done in the direction of analyzing situations where compact objects can mimic black hole shadows through effects associated to its astrophysical neighbourhood, such as accretion. Boson stars have been studied in this context in [133], showing that they can imitate the behaviour of a Kerr shadow without presenting a light ring by producing dark inner regions in the initial accretion configuration. This idea was studied further in [96], where GRMHD simulations and synthetic image reconstructions were performed in order to establish a methodology to differentiate black holes from boson stars.

For Proca stars, it has been shown that some solutions can attain a maximum angular velocity along the timelike circular orbits, producing an inner edge that can resemble the horizon of black hole [59]. By considering a modified potential including a self-interaction term

$$V = \frac{\mu_P}{2} \mathbf{A}^2 + \frac{\lambda_P}{4} \mathbf{A}^4 \quad (83)$$

the authors study several configurations along the whole space of solutions which could give rise to the effect described in the previous lines. However, when considering self-interactions these solutions fall within a perturbatively unstable regime, thus it is needed to assume $\lambda_P = 0$. A special solution, which is denoted by the dot in figure 5, with the parameters

$$\omega/\mu_P \simeq 0.936, \quad M\mu_P = 0.925 \quad (84)$$

has maximum angular velocity located at the radius R_Ω , this acts as an analogous of the innermost stable circular orbit (ISCO) in Schwarzschild black holes. This is an stable solution that emulates a Schwarzschild shadow due to a centrifugal barrier produced by the violation of the condition shown in eq. (85).

In the same work, the authors applied ray-tracing techniques in order to reconstruct the path followed by light rays from the observers backwards to the source by integrating the null geodesic equations. The results show a disk with its inner surface located at the radius associated to the maximum angular momentum $R_\Omega = 6M$, which is the same radius associated to Schwarzschild ISCO.

The angle at which the simulations were made resemble the same angle between the Earth and the source observed by the Event Horizon Telescope

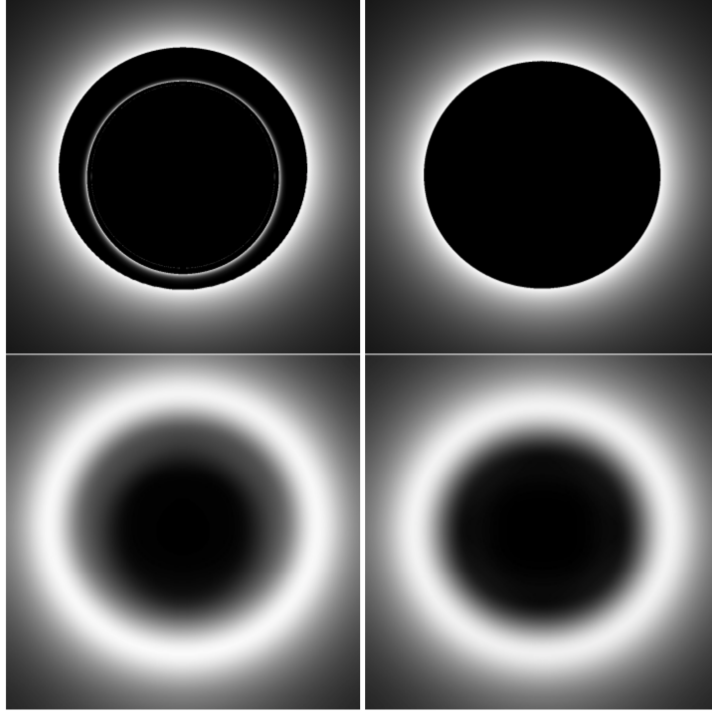


Figure 8: Comparison between lensing from Schwarzschild and Proca special solution [59].

Collaboration (EHTC) [9]. The density and luminosity profile associated this disk in the simulations shown in figure 8 are such that the maximum is shown in the inner edge of the disk. Also, an image reconstructed with the same resolution as the observations available within the limits of the EHTC is shown. In this resolution, both shadows share great resemblance, however, when observing from another angle, several differences are notable. This fact, however, raises the question about how to differentiate black holes from other compact objects, as the angle of observation cannot be chosen.

A good alternative to further study the hypothesis proposed by [59], is to study Proca stars in the context of accretion by means of GRMHD simulations in a similar way as has been done for scalar boson stars in [96]. This will allow to determine if Proca stars can really mimic black holes in an ideal astrophysic setup before exploring more complicated and realistic cases, such as a rotating Proca star.

5. Accretion

Accretion is a very physically rich process which combines the framework from general relativity, electrodynamics and plasma physics. The process consists in the astrophysical environment of a compact object being pulled into a central gravitational well produced by the self-gravity of the object. When the central object is a black hole, some of the matter is going to be captured into the horizon, while the rest, stays in orbit around the object, producing an accretion disk.

5.1. Accretion flows around compact objects

Accretion flows are present in a broad range of astrophysical systems and scales, from galactic nuclei to binary systems of compact objects. Accretion is one of the most efficient methods to obtain energy due to the wide variety of processes that occur into the accreting material. The accreting gas is usually conformed by electrons and ions which exist under the influence of magnetic fields; this rich structure allows for interactions that make plausible for fluid dynamics to be applied to this problem.

In an accretion scenario, bremsstrahlung and synchrotron radiation appear. The radiated power for the first kind of radiation is around 10^{17} *ergs/sec*, while for synchrotron, the power is several order of magnitudes higher, at around 10^{29} *ergs/sec*, although, when referring to black holes, most of this radiation comes from near horizon zones [89].

Another type of radiation comes from Compton scattering, where the outgoing photons exert a force on the accreting gas, reducing the inflow into the compact object and consequently the mass accretion rate. This force must be balanced with the gravitational pull in order to obtain a system in hydro static equilibrium. This limit is known as the Eddington limit. After the photon pressure wins over gravity, the mass accretion rate starts to decrease until gravity takes over, creating a self-regulated system [95].

Accretion flows can be classified according to their mass accretion rate into cold and hot flows. This classification is also reflected on the optic properties of the orbiting gas, as for cold flows, the gas is cooler and optically thick due to the higher accretion rate and are usually found in active galactic nuclei (AGN) and binary systems, while on the other hand, hot flows are the predominant configurations for black holes. They present a lower accretion rate, forming an optically thin disk with usually lower radiative efficiency [137].

The physics of accretion consists on studying the conservation equations that are described by GRMHD coupled with equations describing the radiation

processes that occur inside the flow [67]. There are multiple solutions to these problems which consider different effects, the classical solution, which considers spherical and radial accretion is known as Bondi accretion [22]. The general relativistic generalization, which considers a polytropic equation of state, is known as Michel accretion [87]. These solutions, however, do not consider the influence of the magnetic fields associated to the accretion disc nor the angular momentum from the parcels of material in the flow.

The first case where angular momentum transport was considered, consisted on a cold accretion flow, known as the thin disk model, which is broadly studied in several references [120, 95]. This model consists in matter orbiting around the central object and getting closer to it by the loss of angular momentum due to viscous dissipation. Usually this approximation is valid when considering below Eddington limit systems. When approaching this limit, the thin disk becomes a slim disk, becoming optically thicker.

The first hot flow model, consisted of hotter accreting material and introduced a two-temperature plasma, considering the different temperatures of ions and electrons, being the first ones much hotter than the latter [121]. This model, although successful in describing some observations, was thermally unstable, however, these instabilities were fixed by introducing advection in the model. In advection models, the energy is not radiated away from the plasma, instead it is kept in the flow, heating it further [63].

Realistic astrophysical accretion flows rely heavily on the effects produced by the magnetic fields, in fact, these fields are the ones responsible for the exchange of angular momentum throughout the flow (magnetorotational instability). For this reason, when modelling accretion problems, the initial magnetic field is important.

In the presence of magnetic fields, there are two main models, the first, known as the magnetically arrested disk (MAD) [91], consists in magnetic field that gets trapped in the surrounding region of the compact object due to the pressure produced by the accretion. As the field keeps accumulating around the central object, it gets trapped and after reaching a special radius, the accretion process gets disrupted. Inside this radius, the accretion flow stops being continuous and is divided into shapeless parcels that continue its way towards the central object by fighting against magnetic re-connections which reduce the velocity of the infalling gas.

Before reaching the MAD limit, the system experiences standard and normal evolution (SANE), providing several structural differences [93]. During the SANE, the magnetic fields do not influence the dynamics of the gas, instead their only function is to transport angular momentum via the magnetorotational instability (MRI), which is discussed in section 5.2.

The SANE and MAD configurations are not exclusive to black holes, as the behaviour is not dependent on the event horizon, the same treatment is applicable to stars, and compact objects in general. By this premise, a natural question arises regarding accretion in neutron stars or white dwarfs and if it can be distinguished from the accretion in black holes or other compact objects. The answer is that all of these cases present different luminosity due to the predominance of different emission processes, and neutron stars usually reach the MAD limit faster [74].

5.2. Magnetorotational instability

The MRI is the mechanism responsible for transporting angular momentum in accretion flows [17]. Originally proposed in the context of accretion disks in [15], one of the main results of considering the MRI is that the weak magnetic fields combined with the rotation of the flows in which the fields are present, are the generators of turbulence on this systems by giving rise to a time-growing instability.

In order to understand the essence of the MRI, it is useful to take into account the fact that the magnetic fields in the accretion flow can be seen as an analogous system of a spring connecting two masses (these masses resemble two parcels of the flow). A system like this, that rotates with respect to a central object, is subject to a torque, which produces a linear instability when considering deviations from circular orbits due to the reduction of angular velocity along the radial direction. The parcel that orbits in the smaller radius decreases its angular momentum due to the torque produced by the spring-like force, and as a consequence, the parcel is sent into a lower orbital radius in order to account for the loss of angular momentum.

Considering a fluid element into the accretion flow, in the presence of a weak magnetic field with harmonic spatial dependence, the frequency ω follows a relation given in terms of a quadratic equation for ω^2 , from where, in order to preserve stability, the following condition must be met

$$\frac{d\Omega^2}{dR} \geq 0. \tag{85}$$

Flows that violate the condition shown in eq. (85) are prone to present the magnetorotational instability. It is interesting to note that such instability is attainable when the magnetic field is weak, which turns out to be the case of most astrophysical flows. The calculations needed to obtain the previous condition is shown in great detail on [16].

5.3. Thick tori as initial condition

In astrophysical realistic scenarios, accretion is not spherical. Deviations from the spherical regime arise when the centrifugal forces present in the accretion process become dominant over the pressure gradients. However, circular orbits are important in this context, as they are necessary to describe fluids around a compact object.

Following [106], in these circular orbits for a generally rotating object with stationary and axisymmetric Killing vectors η^μ and ξ^μ , there is no radial, nor poloidal velocity, such that the four-velocity is given in terms of the angular velocity and the Killing vector, as

$$u^\mu = u^t(\eta^\mu + \Omega \xi^\mu), \quad \text{with} \quad \Omega = \frac{u^\phi}{u^t}. \quad (86)$$

Through the normalization condition $u^\mu u_\mu = -1$, the temporal component of the velocity \mathbf{u} can be written as

$$(u^t)^{-2} = -(g_{tt} + 2\Omega g_{t\phi} + \Omega^2 g_{\phi\phi}), \quad (87)$$

From the previous expression, the acceleration of the fluid can be found

$$a_\mu = u^\nu \nabla_\nu u_\mu = \partial_\mu \ln|u_t| - \frac{\Omega}{1 - \Omega l} \partial_\mu l, \quad (88)$$

where l represents the specific dimensionless angular momentum, which fulfills

$$l = \frac{-u_\phi}{u_t}, \quad \text{such that} \quad \frac{l}{1 - \Omega l} = u^t u_\phi. \quad (89)$$

Substituting the acceleration in the Euler equation (obtained for an ideal fluid through the projection of the stress-energy tensor conservation shown in eq. (26 by the use of the projector h^μ_ν):

$$u^\mu \nabla_\mu u_\nu + \frac{1}{\rho h} h^\mu_\nu \nabla_\mu p = 0 \quad \rightarrow \quad \partial_\mu \ln|u_t| - \frac{\Omega}{1 - \Omega l} \partial_\mu l = -\frac{1}{\rho h} \partial_\mu p \quad (90)$$

By deriving this equation and contracting it with the Levi-Civita tensor, and, due to the fact that for barotropic fluids, the enthalpy derivative is proportional to the derivative of the pressure, the angular velocity must contain explicit dependence on the angular momentum. This is known as the relativistic von Zeipel theorem [5], which indicates that for flows circulating around geometries such as the one described above, the surfaces of constant angular velocity and constant angular momentum, are the same. Von Zeipel surfaces are cylinders in

the newtonian regime, while for other, more general geometries, they are only cylinders in the asymptotic limit.

This allows to define this quantities in terms of the metric functions as

$$l(r, \theta) = -\frac{g_{t\phi} + g_{\phi\phi}\Omega}{g_{tt} + g_{t\phi}\Omega} \quad \text{and} \quad \Omega(r, \theta) = -\frac{g_{t\phi} + g_{tt}l}{g_{\phi\phi} + g_{t\phi}l} \quad (91)$$

from where the equation that defines the von Zeipel cylinders can be found to be

$$g_{tt}l + g_{t\phi}(1 + \Omega l) + \Omega g_{\phi\phi} = 0 \quad (92)$$

This theorem holds not only for black holes, but for any compact object that can be written in terms of an stationary and axisymmetric line element.

By using this result, equation (90) can be integrated in terms of exact differentials, such that the integration is path-independent, resulting in

$$\mathcal{W} - \mathcal{W}_{in} = -\int_0^p \frac{dp'}{\rho h} = \ln|u_t| - \ln|(u_t)_{in}| - \int_{l_{in}}^l \frac{\Omega dl'}{1 - \Omega l'} \quad (93)$$

where \mathcal{W} represents the effective potential containing information about the hydrodynamic effects, while the variables containing the subscript "in", represent the values associated to the state where there is no pressure.

The result found in eq. (93) shows that constant pressure surfaces are associated to constant angular momentum surfaces in the equatorial plane. Such surfaces are known as equipotential and they usually present a cusp that marks the inner edge of the toroidal disk. This cusp marks the inner edge of the disk, which is associated to the point where pressure vanishes and is a characteristic of this approach, independent of the angular momentum distribution [4].

It has also been proven that marginally stable disks appear when the angular momentum is kept constant [117]. In this case, the cusp is located between the marginally bound and the marginally stable orbits of a test particle orbiting around the compact object. Under this configuration, the system is completely determined when specifying the constant value of the angular momentum l_0 , the position of the inner edge of the disk and an equation of state (remembering that it must be barotropic for the von Zeipel theorem to hold). When these are provided, the effective potential is determined as

$$\mathcal{W}(r, \theta) = \frac{1}{2} \ln \left(\frac{g_{t\phi}^2 - g_{tt}g_{\phi\phi}}{g_{\phi\phi} + 2l_0g_{t\phi} + l_0^2g_{tt}} \right) \quad (94)$$

All of the accreting material is then enclosed into constant surfaces associated to a specific value of \mathcal{W} , with the boundary being defined by the surface \mathcal{W}_{in} .

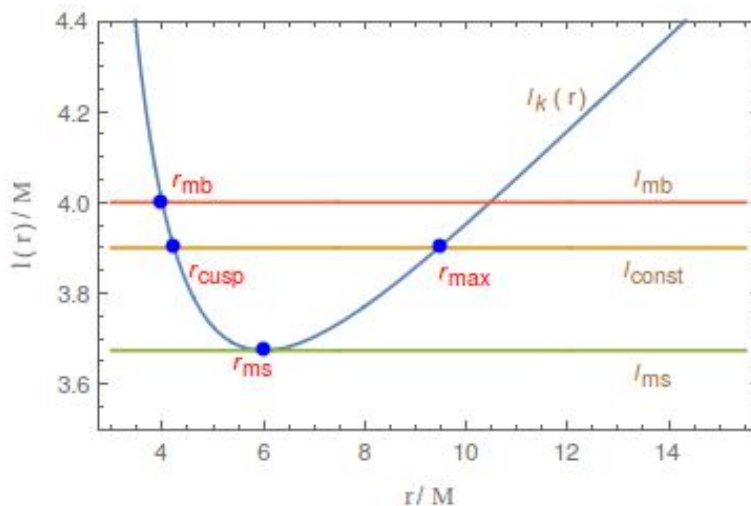


Figure 9: Keplerian angular momentum distribution for Schwarzschild space-time, showing the position of the cusp and the center of the torus.

The choice of the inner edge of the disk is directly related to the shape of the disk. By defining the parameter $\Delta\mathcal{W} = \mathcal{W}_{in} - \mathcal{W}_{cusp}$, different possibilities appear depending on the sign of this value. The first case consists in $\Delta\mathcal{W} < 0$, where the torus is fully localized and in equilibrium, needing a higher energy input than $\Delta\mathcal{W}$ for accretion to start. On the other hand, when $\Delta\mathcal{W} > 0$, mass is transferred through the edge of the disk.

In order to demonstrate the role that the effective potential \mathcal{W} plays regarding the variables of the flow, it is useful to examine the illustrative and commonly found example in the literature of a fluid with a polytropic equation of state in the form $p = K\rho^\Gamma$, in which case, integration of eq. (93) results in [106]

$$\rho(r, \theta) = \left[\left(\frac{\Gamma - 1}{K\Gamma} \right) \left(e^{\mathcal{W}_{in} - \mathcal{W}(r, \theta)} - 1 \right) \right]^{1/(\Gamma-1)}. \quad (95)$$

From eq. (95), it can be noted that the constant \mathcal{W} surfaces are the same as the constant density and pressure (related by the equation of state) surfaces. When observing the surfaces that lay on the equation plane, locally, the minimum of the effective potential corresponds to a maximal pressure/density and it is known as the center of the torus. On the other hand, the maximum value represents the cusp, which is not always present.

The study of thick tori as an initial condition for the problem of accretion has been studied in the context of boson stars [86, 127], showing that anomalous structures that are not present in black holes, can emerge, such as more than one center. Up to this time, there is no such study for the case of Proca stars.

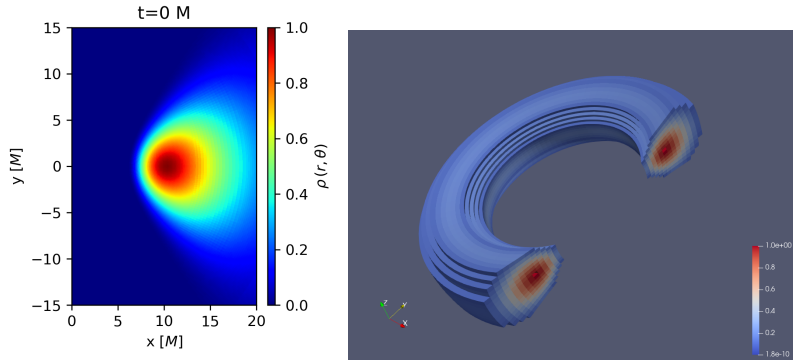


Figure 10: Thick tori as initial condition. Left panel shows a 2D reconstruction, while a 3D torus can be seen in the right panel.

Figure 10 shows the thick tori as initial condition in the study of the accretion problem, in this case, there is no cusp and the torus represents the normalized density of the fluid, with the maximum shown in the center. The compact object around at which the toroidal structure is formed is located at $r = 0$. The variables associated to the fluid are then evolved through the equations of magnetohydrodynamics defined in the previous sections, with the magnetic field being responsible for the exchange of angular momentum (and thus, the accretion of matter into the compact object) via the magnetorotational instability.

6. Numerical simulations of Accretion onto Proca stars

This section consists in explaining the initial data setup of numerical simulations needed to model the evolution of accretion onto Proca stars.

6.1. Physical configuration

As mentioned in section 4.5, the results obtained in [59] (shown in figure 8), do not consider astrophysical effects produced by the environment that surrounds the hypothetical Proca star. This new approach, as the one shown in [96], considers the effects of the surrounding material which accretes into the central object. The process of accretion can then drastically affect the shadow produced by the standard geodesic calculations due to the GRMHD effects that take place due to the accreting material. By studying a 3D reconstruction of the evolution due to the accretion, it would be possible to determine if the results obtained in [59] are relevant enough as to continue the study of these objects.

The simplest configuration of a Proca star is given by the special Proca solution from [23], which consists in considering $F_2(r, \theta) = F_1(r, \theta) = F_1(r)$ and $W(r, \theta) = 0$ in the metric element from eq. (78), while $H_2(r, \theta) = H_3(r, \theta) = 0$ in the potential ansatz from eq. (79). This makes it possible to remove the angular dependence in the functions, resulting in a line element written in terms of isotropic coordinates as

$$ds^2 = -e^{2F_0(r)} dt^2 + e^{2F_1(r)} [dr^2 + r^2(d\theta^2 + \sin^2 \theta d\phi^2)] \quad (96)$$

With respect to the parameter space conformed by the normalized ADM mass and the frequency of the field, the characteristics associated to this special solution, which represents a non-rotating system, are shown in figure 5.

In order to simulate the evolution of the accretion flows that surround the Proca star, the numerical code BHAC is employed, which implements the GRMHD equations (eqs. (25- 28)) together with the necessary conditions for the MRI (discussed in section 5.2) to present itself, taking the thick tori from section 5.3 as an initial condition.

As discussed in section 3.2.1, the equation of state must be specified in order to fully characterize the system. On this account, the accreting plasma follows the equation of state of an ideal gas with an adiabatic index $\gamma = 4/3$. The temperature associated to the accretion disk obligates the electrons and ions confined in the torus to move at relativistic velocities, which requires relativis-

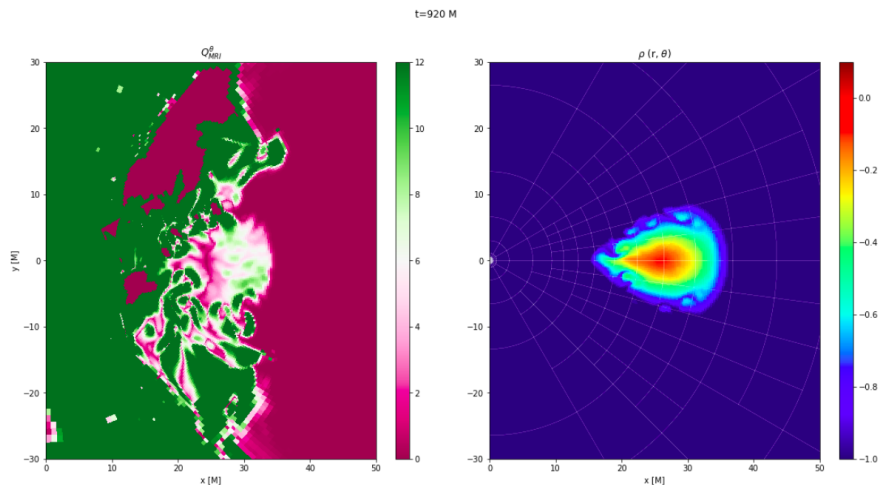


Figure 11: The quality factor along the θ direction is shown on the left panel. Right panel shows the adaptive mesh refinement over each the grid.

tic corrections to be implemented in the equation of state [51]. However, recent results show that when significant changes in velocity are not present, the equation of state can be approximated by an ideal gas with $\gamma \simeq 1.44$ [123], and thus, modelling the accretion flow as a fluid with adiabatic index of $\gamma = 4/3$ does not yield significant differences.

As for the properties of the plasma, the ratio between hydrodynamic pressure and magnetic pressure, known as plasma- β takes a value of 100, showing that the magnetic field is weak compared to the hydro-dynamical effects, which is the required condition for the MRI to appear.

There must be a sufficient level of refinement throughout the numerical grid in order for the MRI to be solved correctly due to the fact that each wavelength up to the fastest growing mode must be captured in order to avoid numerical dissipation that stops the accretion process. This can be quantified through quality factors, given in terms of the wavelengths of the fastest growing mode evaluated in a tetrad lagrangian frame that adopts the corresponding grid resolution [102].

For a given coordinate direction k , the quality factor $Q^{(k)}$ is given by

$$Q^{(k)} = \frac{\lambda^{(k)}}{\Delta x^{(k)}}, \quad (97)$$

where $\lambda^{(k)} = \frac{2\pi b^\mu e_\mu^{(k)}}{\Omega \sqrt{\rho h + b^2}}$ and $\Delta x^{(k)} = \Delta k^\mu e_\mu^{(k)}$

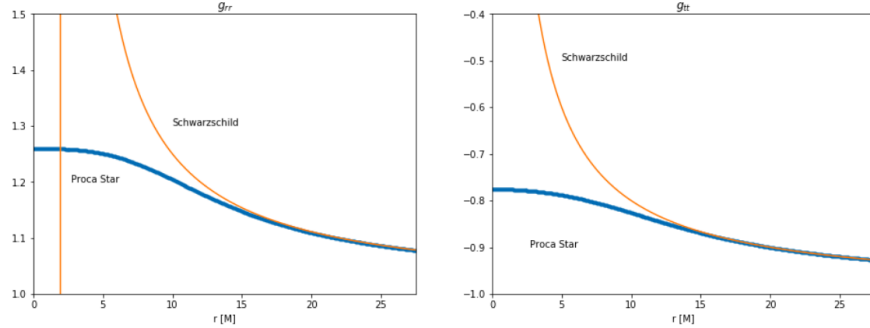


Figure 12: Proca stars line element compared with Schwarzschild, left panel shows the radial metric function g_{rr} , while the temporal metric function can be seen on the right panel.

where $\Delta k^\mu = \Delta k \delta_k^\mu$ is the distance between two adjacent cells in the grid along the coordinate k and $e_\mu^{(k)}$ represents the tetrad basis vector associated to k . The quality factor for the MRI associated to the θ -direction is shown in figure 11 along with the refinement along the grid.

In order to work out the 3 + 1 decomposition of the line element discussed in section 3.1, eq. (96) can be re-expressed into an areal system of coordinates with the form

$$ds^2 = -A(r)dt^2 + B(r)dr^2 + r^2 d\Omega^2 \quad (98)$$

$$A(r) = e^{2F_0(r')}, \quad B(r) = [1 + r' \partial_{r'} F_1(r')]^{-2}$$

This line element is asymptotically flat, such that at long distances, it resembles the Schwarzschild metric, this behaviour is shown in 12. Direct comparison from eq. (98) with eq. (5) shows that

$$\beta_i = 0, \quad \alpha = e^{F_0(r')}, \quad \gamma_{ij} = B(r) \delta_i^r \delta_j^r + r^2 (\delta_i^\theta \delta_j^\theta + \sin^2 \theta \delta_i^\phi \delta_j^\phi) \quad (99)$$

As mentioned before, the code is constructed in such a way that accretion starts with the thick tori condition (see section 5.3). For Proca and Schwarzschild spacetimes, the effective potential associated to the hydro-dynamical effects shown in eq. (94) is given by

$$\begin{aligned} \text{Proca Star:} \quad \mathcal{W}(r) &= \frac{1}{2} \ln \left(\frac{r^2 e^{2F_0(r)}}{r^2 - l_0^2 e^{2F_0(r)}} \right) \\ \text{Schwarzschild:} \quad \mathcal{W}(r) &= \frac{1}{2} \ln \left(\frac{r^2 (r-2)}{r^3 - l_0^2 (r-2)} \right) \end{aligned} \quad (100)$$

The free parameters needed to completely specify the initial conditions of the problem are l_0 and r_{in} , as shown from eq. (93) in the case of constant

angular momentum. The inner radius takes the value of $r_{in} = 18 M$ while the angular momentum is specified in such a way that the minimum value of the potential is fixed at $r_m = 25 M$.

The previous choice of the parameters r_{in} and l_0 is associated to the fact that Proca spacetime converges to a Schwarzschild line element far from the origin as can be seen in figure 12, and thus, the initial condition is qualitatively the same for both geometries, as can be seen in figure 13. This allows for the differences in the evolution of the accreting material in both cases to appear naturally without any previous bias.

6.2. Computational and numerical configuration

BHAC calculates the relevant variables for the accretion problem by using the methods discussed in section 3.2.1. The code calculates the density and the associated thermodynamic quantities such as pressure, entropy and enthalpy, while also calculating dynamic variables such as the fluid velocities and the Lorentz factor. Several other quantities are computed, such as magnetic fields, the plasma beta, the mass accretion rate and the kinetic, thermal and electromagnetic energies, as well as the quality factor.

The simulation lasts $1472736 s \simeq 409 hrs$ running in 8 CPUs. It takes place into a grid with total resolution of 192×96 , three levels of refinement, an outer boundary located at $r = 2500 M$ and a maximal radial spacing of $\sim 3 M$.

In order for the code to show an optimal resolution across all required regions (near the horizon and the equatorial plane) of the grid, modified Kerr-Schild (MKS) coordinates [85, 103] are employed, which consist on a coordinate transformation of the form

$$r_{KS}(s) = R_0 + e^s, \quad \theta_{KS}(\vartheta) = \vartheta + \frac{h}{2} \sin 2\vartheta \quad (101)$$

where s and ϑ represent the original standard spherical coordinates, and the parameters R_0 and h control the resolution associated to each region of the ones mentioned above. In the current case, we consider $R_0 = 1.0$ due to the fact that we are interested in studying the regions where shadows are usually formed in black holes and $h = 0.0$ as we are working with an spherically symmetric configuration.

As mentioned before, the CFL condition, discussed in 3.4.1, must be manually implemented to guarantee a stable evolution [38]. And thus, in this work, we employ a value of 0.7.

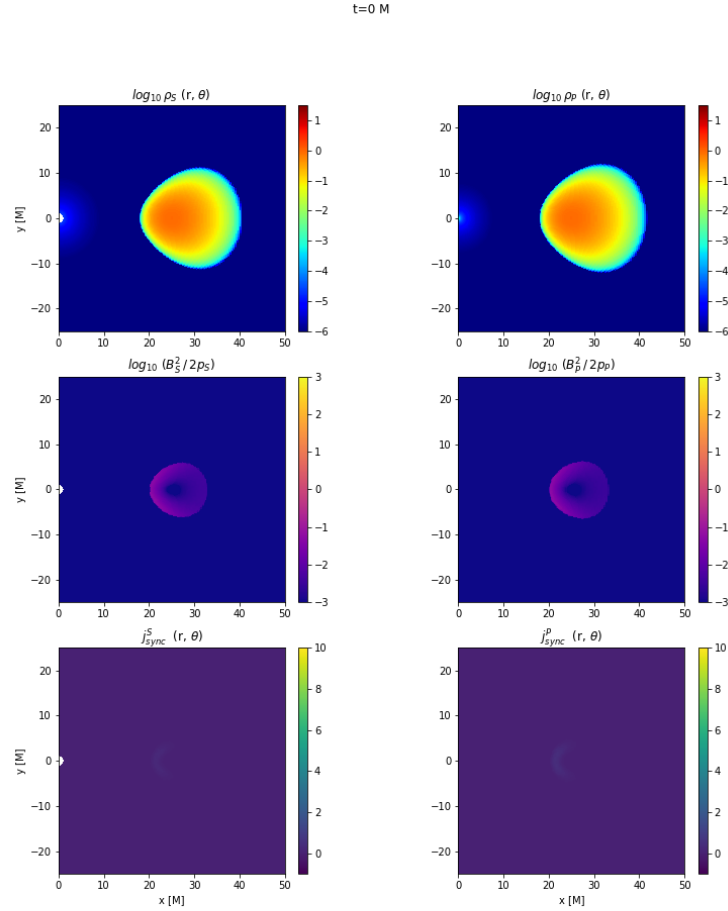


Figure 13: 2D-Evolution of the flow at $t = 0$. The figures on the left side represent a Schwarzschild black hole, while Proca stars are shown on the right. The top row of each panel shows the density of the accretion flow in logarithmic scale. The middle row represents the inverse of plasma-beta, while the lower row shows the luminosity proxy.

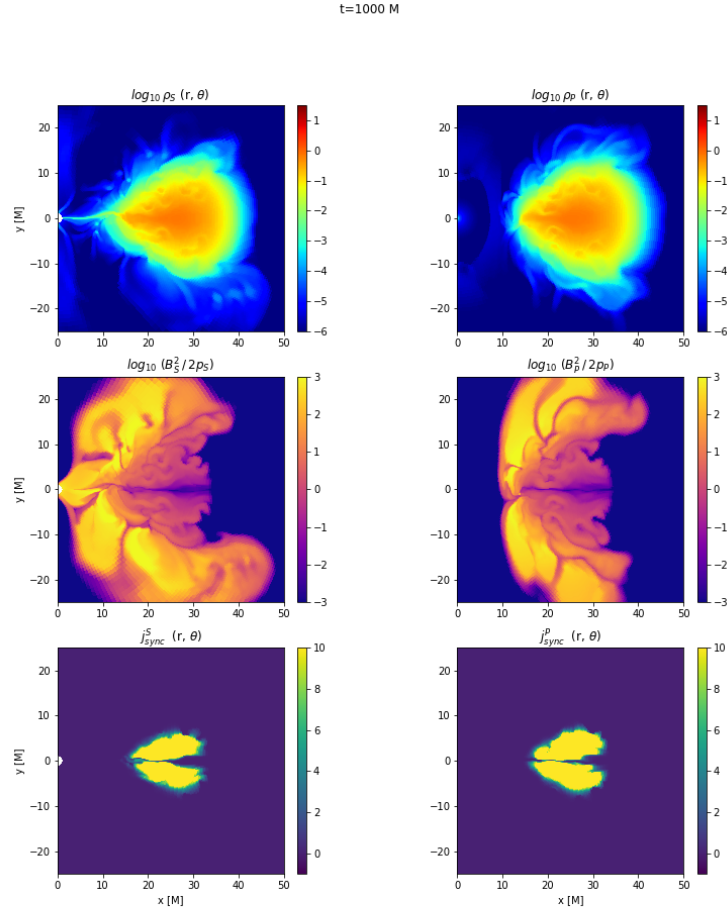


Figure 14: 2D-Evolution of the flow at $t = 1000$. The figures on the left side represent a Schwarzschild black hole, while Proca stars are shown on the right. The top row of each panel shows the density of the accretion flow in logarithmic scale. The middle row represents the inverse of plasma-beta, while the lower row shows the luminosity proxy.

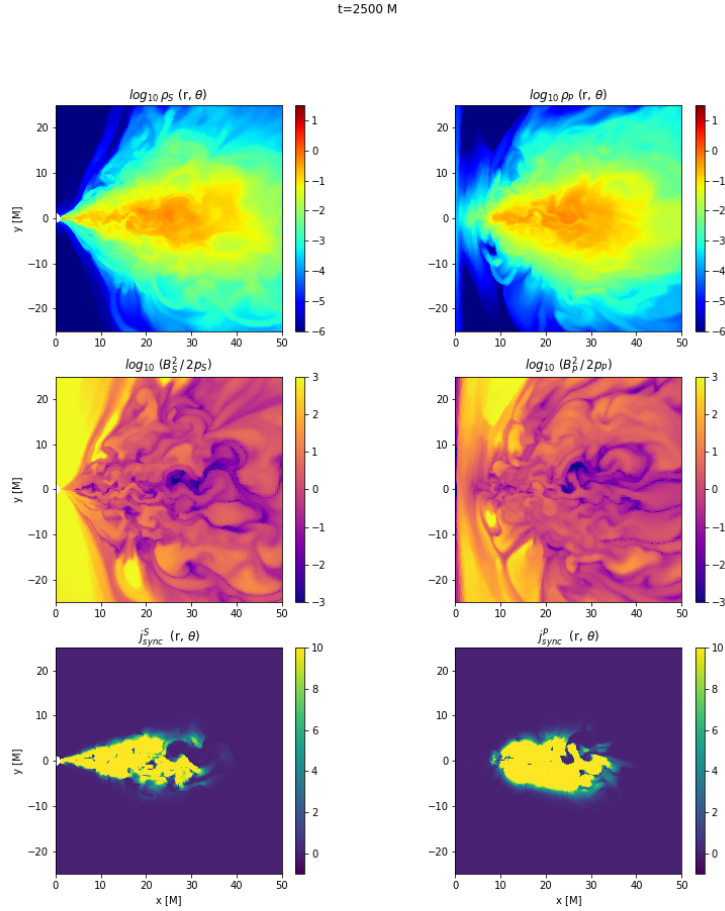


Figure 15: 2D-Evolution of the flow at $t = 2500$. The figures on the left side represent a Schwarzschild black hole, while Proca stars are shown on the right. The top row of each panel shows the density of the accretion flow in logarithmic scale. The middle row represents the inverse of plasma-beta, while the lower row shows the luminosity proxy.

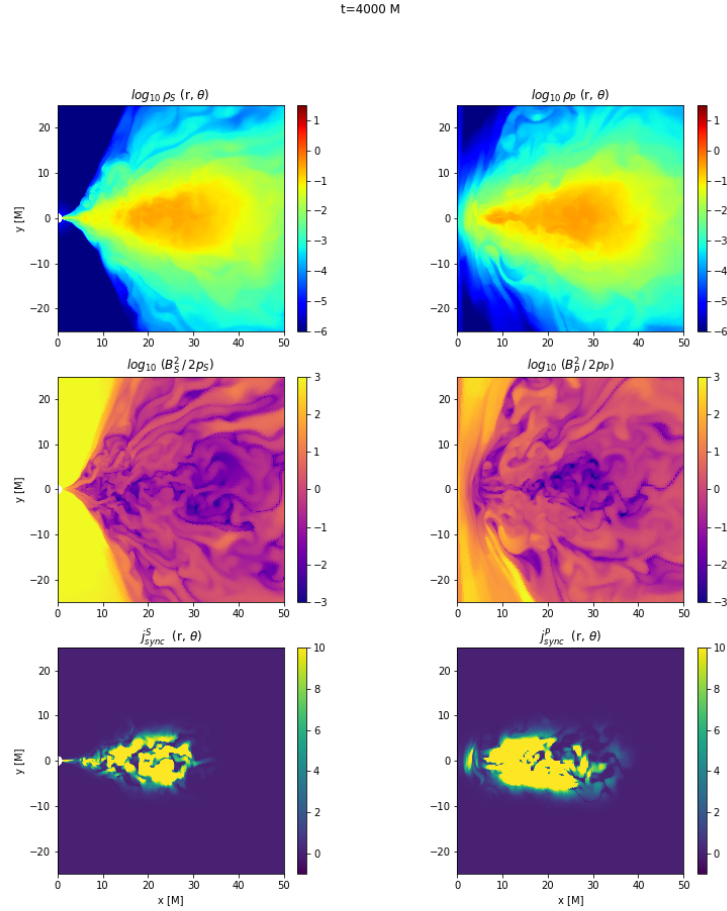


Figure 16: 2D-Evolution of the flow at $t = 4000$. The figures on the left side represent a Schwarzschild black hole, while Proca stars are shown on the right. The top row of each panel shows the density of the accretion flow in logarithmic scale. The middle row represents the inverse of plasma-beta, while the lower row shows the luminosity proxy.

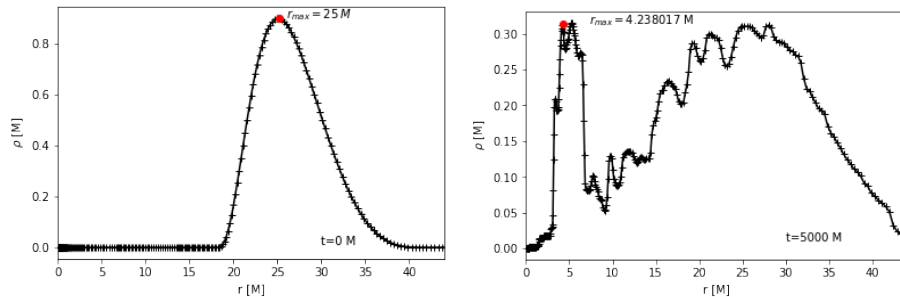


Figure 17: Density profile associated to accretion onto Proca stars. Left panel shows the initial configuration associated to the tori condition, while the right panel shows the density profile at $t = 5000 M$.

6.3. Results

The top panels from figures 13-16 show the evolution of the logarithmic density distribution originally shown in figure 10 for both Schwarzschild (left) and Proca (right) spacetimes at four different temporal instants. The first set shows the initial condition, the second one shows the evolution at $t = 1000 M$, the third at $t = 2500 M$ and the last one shows $t = 4000 M$. It can be seen that since $t \sim 1000 M$, the accreting flow already presents substantial differences regarding horizon-like effects, which in the Schwarzschild case, shows a small funnel representing the material that is flowing into the horizon. On the other hand, for a Proca star, the material accretes into the center through a more chaotic process and in a slower way than for Schwarzschild, this is due to the fact that matter is getting closer to the maximum value of angular velocity, which as discussed on section 5.2, produces the accretion process to be stopped.

The maximum value of angular velocity, however, is displaced further into the center of the object due to the angular momentum interchange produced by the MRI and the related hydrodynamical effects, reaching a maximum value, R_{Ω}^{GRMHD} , around $r_{max} = 4.238 M$. In consequence, the accreting material is halted around this radius preventing the flow to move forward into the center of the star as can be seen from figure 17, which shows the density profile associated to the matter that surrounds the Proca star.

Left panel from figure 17 shows the initial distribution of matter associated to the tori condition, while the right panel shows the density profile at $t = 5000 M$, from where it can be observed that the material does not go into the center, instead, it accumulates around r_{max} . This can produce the effect of a shadow in some observations due to the fact that there is no baryonic matter into the center and the Proca particles that conform the star do not interact with electromagnetic radiation, creating an effective representation of a central dark

region surrounded by the bright accreting material.

The middle panel from figures 13-16, represent the inverse of the plasma- β , showing which regions are dominated by hydrodynamical pressure and which ones by magnetic pressure. In this case, inside the torus, hydrodynamic pressure is dominant along most of the evolution process in contrast to the effects associated to the magnetic field.

The bottom panel from figures 13-16 represent the emission proxy associated to thermal synchrotron radiation, as given in [102]. This is represented by the emissivity j , which has the form

$$j = \frac{\rho^3}{p^2} e^{-C \left(\frac{\rho^2}{Bp^2} \right)^{1/3}} \quad (102)$$

where the constant C measures the radiation cutoff needed to resemble the emission spectra from this sources. As discussed on [102], in order to model an optically thin emission flow coming from a galactic center, which emits in the milimeter wavelength band that the EHT observes, $C = 0.2$. This proxy is useful regarding the reconstruction of synthetic optical observations.

Regarding the emission proxy from both astrophysical objects (Proca star and Schwarzschild black hole), differences do not appear during the early stages of the evolution, however, after the material gets further into the near-horizon zone for the black hole, notable visual differences appear. This is due to two principal reasons, the first one is that accretion into a black hole is characterized (in this case) by a flow that is collimated when going through the horizon, this material never stops emitting. The second reason is the fact that the material from the Proca star does not cross r_{max} , creating an effective dark region absent of synchrotron radiation.

This analysis shows that although Proca stars and Schwarzschild black holes are fairly different when studied under the problem of accretion, Proca stars can act as black hole mimickers in specific cases due to the fact that they can present a dark inner region. The formation of this region is dependent only on the existence of a maximal angular velocity, which as shown in [59], occurs for several radii. This, in turn, depends directly on the parameters of the solution to the Einstein-Proca system. This allows for the radius at which the maximal angular velocity appears (R_Ω) to be expressed in terms of the amplitudes associated to the Proca field from eq. (73) (as shown in figure 18).

Figure 17 shows that through GRMHD simulations, the radius R_Ω is displaced into an inner orbit. This behaviour can be generalized to different Proca stars by considering that the GRMHD effects manifest themselves through the complete branch of solutions which allow a maximal angular velocity. This makes it possible to define a region of influence associated to GRMHD effects through this set of solutions, as can be seen in figure 18, where the radius of

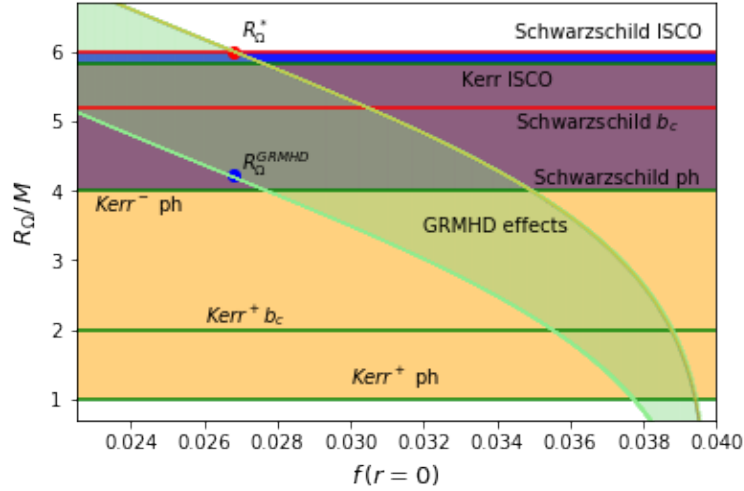


Figure 18: Radius of maximum angular velocity as a function of the Proca field amplitude

maximal velocity is expressed in terms of the radial amplitude of the Proca field, as given in eq. (73), at the origin of coordinates. The same figure shows the regions of intersection with relevant orbits associated to Schwarzschild and Kerr black holes, showing that all of these orbits fall within the region of interest of Proca stars, and thus, allowing for a Proca star to mimick the shadow casted by these black holes. It is important to notice that the dark region formed in the Proca case is due to hydrodynamical effects in contrast with the gravitational deformation of orbits produced in black holes.

7. Discussion and Conclusions

This work studied by the means of numerical simulations, the effect of GRMHD effects on Proca stars that produce a dark inner region, with the goal of determining if these can be observationally confused with the shadow of a black hole in a more realistic astrophysical scenario.

In order to better quantify the differences between both compact objects, the simulations done in this work use the same initial configuration. These differences are produced by two factors, the first one is the non-existence of an event horizon in the case of the Proca star, which in the absence of angular velocity peaks, allow for matter to be accreted all the way to the center of the star (which is also surface-less). In black holes, the presence of an horizon produces a funnel which controls the flow of matter that crosses into the horizon. This is not present in the case of Proca stars, so that the accretion pattern shown in the simulation is more chaotic in this case. The second factor, is that Proca stars (along the branch of solutions presented) exhibit a maximum angular velocity, which suppresses the MRI, and thus, the accretion, producing a dark inner region. Due to the fact that this phenomena appears at several radii depending on the parameters of the solution, the apparent size of this region can take different values that overlap with the size of a Schwarzschild or Kerr black hole.

By considering the effects of GRMHD in the simulations, the originally calculated radius where the maximal angular velocity appears is shifted further into the center. After reaching this radius, matter is shoved inwards, accumulating itself and presenting a peak in the density profile at $r_{max} = 4.238 M$. The inner region delimited by this radius is displayed as a dark area that emulates the shadow of a black hole. However, for a Proca star to mimic a black hole of the same mass, the maximum value of angular velocity must be higher than the one proposed in [59] due to the GRMHD effects.

In order to gain insight regarding the problem of a black hole shadow being emulated by a Proca star, synthetic images must be constructed to gain insight about the observational results that could be obtained by experiments such as the EHT. More simulations from different Proca solutions are also needed in order to study the modifications produced by the GRMHD effects.

The work presented here can be summarized by the following statements:

- Proca stars present a maximum value of angular velocity which suppresses the accretion-driven processes, producing a dark area on the inner region of the star resembling the effect of shadows in black holes.
- The influence of GRMHD effects is reflected on the fact that the radius at which the angular momentum transport is suppressed is moved inwards,

resulting in a smaller dark region with respect to the original calculation. However, the radius that delimits this region can match several structures that can be found in a black hole anatomy depending on the Proca field amplitude.

- The analysis presented in this work indicates that Proca stars can, theoretically, mimic black holes under certain specific conditions. However, more work is required in order to narrow the space of parameters that allow for this phenomena to appear. This involves working with different solutions to the Proca-Einstein system presented in [23], in order to narrow the window of theoretical degeneration produced by GRMHD effects shown in figure 18.
- Regarding the observational degeneration, radiation detected by VLBI is mostly from synchrotron emission (around mm-wavelengths), thus, reconstructed synthetic images from VLBI observations are needed in order to assert whether a Proca star can be an observational emulator of a black hole. The construction of such images requires further simulations with the inclusion of radiative transfer calculations.

8. Appendix A: Cauchy problem and hyperbolic systems

The hyperbolic character of the GRMHD equations (40) is a key factor for such systems of equations to be solved. This section aims to give a brief introduction to the basic properties needed in a system for it to be hyperbolic.

8.1. Partial differential equations and the Cauchy problem

A partial differential equation (PDE) of order m has the general form

$$\sum_{|j| \leq m} a_j(x) D^j u = f \quad (103)$$

where a_j , u and f represent functions of the coordinate set x , and D^j is a partial differential operator acting over the set of functions u . The principal part of a partial differential equation is given by

$$\sum_{|j|=m} a_j D^j \quad (104)$$

Eq. (103) is greatly simplified for the case of N first-order equations, as the principal part can be written in terms of matrix elements [34].

The Cauchy problem for a PDE consists on finding a C^m -class solution for eq. (103), which, along with their respective $m - 1$ lowest order derivatives, take fixed values that are constrained into a $n - 1$ dimension manifold (a sub-manifold known as characteristic manifold) [33]. The differential equation, on this manifold S satisfies a first order equation

$$\sum_{|j|=m} a_j p^j = 0, \quad \text{with} \quad p^J = \prod_{k=1}^n \left(\frac{\partial S}{\partial x^k} \right)^{J_k} \quad (105)$$

from PDEs can be classified into elliptic, hyperbolic or parabolic into a specific direction according the corresponding solutions for the principal part of the equation, which is directly related to the structure of the manifold.

Due to the nature of this work, the analysis is focused only on hyperbolic systems, however, the interested reader can find the classification and expand these ideas in [33].

Hyperbolic equations then are obtained when the eigenvalues associated to the principal part are all real. Hyperbolicity of these equations can appear in a

strong or weak regime. Weak hyperbolicity consists only in having real eigenvalues, while the strong regime appears when these eigenvalues form complete sets of eigenvectors [60]. The matrix associated to the principal part of the PDE can be symmetric, in which case, it is automatically strongly hyperbolic. Strong hyperbolicity is needed in order to guarantee the well-posedness of the system. The eigenvalues associated to the matrix define the propagation speed of information related to these systems. The most commonly-known hyperbolic equation is the wave equation.

References

- [1] B. P. Abbott et al. «Observation of Gravitational Waves from a Binary Black Hole Merger». In: *Phys. Rev. Lett.* 116 (6 2016), p. 061102. DOI: 10.1103/PhysRevLett.116.061102. URL: <https://link.aps.org/doi/10.1103/PhysRevLett.116.061102>.
- [2] R. Abbott et al. «GW190521: A Binary Black Hole Merger with a Total Mass of $150 M_{\odot}$ ». In: *Phys. Rev. Lett.* 125 (10 Sept. 2020), p. 101102. DOI: 10.1103/PhysRevLett.125.101102.
- [3] K. Abramowicz, M. Jaroszynski, and M. Sikora. «Relativistic, Accreting disks». In: *Astron. Astrophys.* 63 (1978), pp. 221–224.
- [4] M. Abramowicz, M. Jaroszynski, and M. Sikora. «Relativistic, accreting disks.» In: *Astron. Astrophys.* 63 (Feb. 1978), pp. 221–224.
- [5] M. A. Abramowicz. «The Relativistic von Zeipel’s Theorem». In: *ACTA ASTRONOMICA* 21 (Jan. 1971), p. 81.
- [6] Abramowicz, M. A., Kluźniak, W., and Lasota, J.-P. «No observational proof of the black-hole event-horizon». In: *A&A* 396.3 (2002), pp. L31–L34. DOI: 10.1051/0004-6361:20021645.
- [7] Kazunori Akiyama et al. «First M87 Event Horizon Telescope Results. II. Array and Instrumentation». In: *Astrophys. J. Lett.* 875.1 (2019), p. L2. DOI: 10.3847/2041-8213/ab0c96.
- [8] Kazunori Akiyama et al. «First M87 Event Horizon Telescope Results. V. Physical Origin of the Asymmetric Ring». In: *Astrophys. J. Lett.* 875.1 (2019), p. L5. DOI: 10.3847/2041-8213/ab0f43.
- [9] The Event Horizon Telescope Collaboration et al. «First M87 Event Horizon Telescope Results. I. The Shadow of the Supermassive Black Hole». In: *Astrophys. J. Lett.* 875 (2019), p. L1. DOI: 10.3847/2041-8213/ab0ec7. arXiv: 1906.11238 [astro-ph.GA].
- [10] Alireza Allahyari et al. «Magnetically charged black holes from non-linear electrodynamics and the Event Horizon Telescope». In: *JCAP* 02 (2020), p. 003. DOI: 10.1088/1475-7516/2020/02/003. arXiv: 1912.08231 [gr-qc].
- [11] D. L. T. Anderson and G. H. Derrick. «Stability of Time-Dependent Particlelike Solutions in Nonlinear Field Theories. I». In: *Journal of Mathematical Physics* 11.4 (1970), pp. 1336–1346. DOI: 10.1063/1.1665265.
- [12] N. Andersson and G. L. Comer. «Relativistic fluid dynamics: Physics for many different scales». In: *Living Rev. Rel.* 10 (2007), p. 1. DOI: 10.12942/lrr-2007-1. arXiv: gr-qc/0605010.
- [13] Luis Anton et al. «Numerical 3+1 General Relativistic Magnetohydrodynamics: A Local Characteristic Approach». In: *The Astrophysical Journal* 637.1 (2006), pp. 296–312. DOI: 10.1086/498238.

- [14] Richard L. Arnowitt, Stanley Deser, and Charles W. Misner. «The Dynamics of general relativity». In: *Gen. Rel. Grav.* 40 (2008), pp. 1997–2027. DOI: 10.1007/s10714-008-0661-1. arXiv: gr-qc/0405109.
- [15] Steven A Balbus and John F Hawley. «A powerful local shear instability in weakly magnetized disks. I-Linear analysis. II-Nonlinear evolution». In: *The Astrophysical Journal* 376 (1991), pp. 214–233.
- [16] Steven A. Balbus. «Enhanced Angular Momentum Transport in Accretion Disks». In: *Annual Review of Astronomy and Astrophysics* 41.1 (2003), pp. 555–597. DOI: 10.1146/annurev.astro.41.081401.155207.
- [17] Steven A. Balbus and John F. Hawley. «Instability, turbulence, and enhanced transport in accretion disks». In: *Rev. Mod. Phys.* 70 (1 Jan. 1998), pp. 1–53. DOI: 10.1103/RevModPhys.70.1.
- [18] Francesc Banyuls et al. «Numerical $\{3 + 1\}$ General Relativistic Hydrodynamics: A Local Characteristic Approach». In: *The Astrophysical Journal* 476.1 (1997), pp. 221–231. DOI: 10.1086/303604.
- [19] Thomas W. Baumgarte and Stuart L. Shapiro. «Numerical integration of Einstein’s field equations». In: *Phys. Rev. D* 59 (2 Dec. 1998), p. 024007. DOI: 10.1103/PhysRevD.59.024007.
- [20] Stuart Boersma and Tevian Dray. «Parametric manifolds. I. Extrinsic approach». In: *Journal of Mathematical Physics* 36.3 (1995), pp. 1378–1393. DOI: 10.1063/1.531127.
- [21] S Bonazzola and J A Marck. «Astrophysical Sources of Gravitational Radiation». In: *Annual Review of Nuclear and Particle Science* 44.1 (1994), pp. 655–717. DOI: 10.1146/annurev.ns.44.120194.003255.
- [22] H. Bondi. «On Spherically Symmetrical Accretion». In: *Monthly Notices of the Royal Astronomical Society* 112.2 (Apr. 1952), pp. 195–204. ISSN: 0035-8711. DOI: 10.1093/mnras/112.2.195.
- [23] Richard Brito et al. «Proca stars: Gravitating Bose–Einstein condensates of massive spin 1 particles». In: *Physics Letters B* 752 (2016), pp. 291–295. ISSN: 0370-2693. DOI: <https://doi.org/10.1016/j.physletb.2015.11.051>.
- [24] Avery E. Broderick et al. «Testing the No-Hair Theorem with Event Horizon Telescope Observations of Sagittarius A». In: *Astrophys. J.* 784 (2014), p. 7. DOI: 10.1088/0004-637X/784/1/7. arXiv: 1311.5564 [astro-ph.HE].
- [25] Juan Calderón Bustillo et al. «GW190521 as a Merger of Proca Stars: A Potential New Vector Boson of 8.7×10^{-13} eV». In: *Phys. Rev. Lett.* 126.8 (2021), p. 081101. DOI: 10.1103/PhysRevLett.126.081101. arXiv: 2009.05376 [gr-qc].
- [26] Max Camenzind. *Compact objects in astrophysics : white dwarfs, neutron stars, and black holes*. 2007. DOI: 10.1007/978-3-540-49912-1.

- [27] Vitor Cardoso et al. «Light rings as observational evidence for event horizons: Long-lived modes, ergoregions and nonlinear instabilities of ultracompact objects». In: *Phys. Rev. D* 90 (4 Aug. 2014), p. 044069. DOI: 10.1103/PhysRevD.90.044069.
- [28] Mani Chandra et al. «AN EXTENDED MAGNETOHYDRODYNAMICS MODEL FOR RELATIVISTIC WEAKLY COLLISIONAL PLASMAS». In: *The Astrophysical Journal* 810.2 (2015), p. 162. DOI: 10.1088/0004-637x/810/2/162.
- [29] S. Chandrasekhar. «The Maximum Mass of Ideal White Dwarfs». In: *APJ* 74 (July 1931), p. 81. DOI: 10.1086/143324.
- [30] Patrick Chi-Kit Cheong, Lap-Ming Lin, and Tjonnie Guang Feng Li. «Gmunu: toward multigrid based Einstein field equations solver for general-relativistic hydrodynamics simulations». In: *Classical and Quantum Gravity* 37.14 (2020), p. 145015. DOI: 10.1088/1361-6382/ab8e9c.
- [31] Cecilia Chirenti and Luciano Rezzolla. «Did GW150914 produce a rotating gravastar?» In: *Phys. Rev. D* 94 (8 2016), p. 084016. DOI: 10.1103/PhysRevD.94.084016. URL: <https://link.aps.org/doi/10.1103/PhysRevD.94.084016>.
- [32] Cecilia B. M. H. Chirenti and Luciano Rezzolla. «How to tell a gravastar from a black hole». In: *Class. Quant. Grav.* 24 (2007), pp. 4191–4206. DOI: 10.1088/0264-9381/24/16/013. arXiv: 0706.1513 [gr-qc].
- [33] Y Choquet-Bruhat. *Analysis, Manifolds and Physics, Part I-Revised and Enlarged Edition*. 2000. ISBN: 9780080527154.
- [34] Yvonne Choquet-Bruhat. *Introduction to General Relativity, Black Holes, and Cosmology*. Oxford University Press, Nov. 2014.
- [35] CmPA. *MPI - Adaptive Mesh Refinement - Versatile Advection Code*. Version 2.2. URL: <http://amrvac.org/index.html>.
- [36] Phillip Colella and Paul R Woodward. «The Piecewise Parabolic Method (PPM) for gas-dynamical simulations». In: *Journal of Computational Physics* 54.1 (1984), pp. 174–201. ISSN: 0021-9991. DOI: [https://doi.org/10.1016/0021-9991\(84\)90143-8](https://doi.org/10.1016/0021-9991(84)90143-8).
- [37] Arthur Congdon and Charles Keeton. *Principles of Gravitational Lensing: Light Deflection as a Probe of Astrophysics and Cosmology*. Springer International Publishing, Mar. 2018.
- [38] R. Courant, K. Friedrichs, and H. Lewy. «On the Partial Difference Equations of Mathematical Physics». In: *IBM Journal of Research and Development* 11.2 (1967), pp. 215–234. DOI: 10.1147/rd.112.0215.
- [39] Pedro V. P. Cunha, Emanuele Berti, and Carlos A. R. Herdeiro. «Light-Ring Stability for Ultracompact Objects». In: *Phys. Rev. Lett.* 119 (25 Dec. 2017), p. 251102. DOI: 10.1103/PhysRevLett.119.251102.

- [40] S. F. Davis. «Simplified Second-Order Godunov-Type Methods». In: *SIAM Journal on Scientific and Statistical Computing* 9.3 (1988), pp. 445–473. DOI: 10.1137/0909030.
- [41] Hooman Davoudiasl and Peter B. Denton. «Ultralight Boson Dark Matter and Event Horizon Telescope Observations of M87*». In: *Phys. Rev. Lett.* 123 (2 2019), p. 021102. DOI: 10.1103/PhysRevLett.123.021102. URL: <https://link.aps.org/doi/10.1103/PhysRevLett.123.021102>.
- [42] A. Dedner et al. «Hyperbolic Divergence Cleaning for the MHD Equations». In: *Journal of Computational Physics* 175.2 (2002), pp. 645–673. ISSN: 0021-9991. DOI: <https://doi.org/10.1006/jcph.2001.6961>.
- [43] Fabrizio Di Giovanni et al. «Dynamical bar-mode instability in spinning bosonic stars». In: *Phys. Rev. D* 102 (12 Dec. 2020), p. 124009. DOI: 10.1103/PhysRevD.102.124009.
- [44] Fabrizio Di Giovanni et al. «Dynamical formation of Proca stars and quasistationary solitonic objects». In: *Phys. Rev. D* 98 (6 Sept. 2018), p. 064044. DOI: 10.1103/PhysRevD.98.064044.
- [45] Gourgoulhon E. *3+1 formalism in General Relativity: Bases of Numerical Reality*. Springer, 2012.
- [46] J. A. Font. «Numerical Hydrodynamics and magnetohydrodynamics in general relativity». In: *Living Rev. Relativ.* 11.7 (2008).
- [47] José A. Font. «An introduction to relativistic hydrodynamics: theory, numerics, and astrophysical applications.» VII Mexican School on Gravitation and Mathematical Physics. 2006. URL: http://pelusa.fis.cinvestav.mx/tmatos/LaSumA/LaSumA2_archivos/RelatividadNum/Font.pdf.
- [48] José A. Font. «General relativistic hydrodynamics and magnetohydrodynamics and their applications». In: *Plasma Physics and Controlled Fusion* 47.12B (Dec. 2005), B679–B690. DOI: 10.1088/0741-3335/47/12B/S50.
- [49] Helmut Friedrich. «Evolution equations for gravitating ideal fluid bodies in general relativity». In: *Phys. Rev. D* 57 (4 Feb. 1998), pp. 2317–2322. DOI: 10.1103/PhysRevD.57.2317.
- [50] Charles F. Gammie, Jonathan C. McKinney, and Gabor Toth. «HARM: A Numerical Scheme for General Relativistic Magnetohydrodynamics». In: *The Astrophysical Journal* 589.1 (2003), pp. 444–457. DOI: 10.1086/374594.
- [51] RP Geroch and DJ Hegyi. «Relativistic equations of state». In: *Nature* 215.5100 (1967), pp. 501–501.
- [52] Steven B. Giddings. «Searching for Quantum Black Hole Structure with the Event Horizon Telescope». In: *Universe* 5.9 (2019). DOI: 10.3390/universe5090201.

- [53] Minyong Guo, Niels A. Obers, and Haopeng Yan. «Observational signatures of near-extremal Kerr-like black holes in a modified gravity theory at the Event Horizon Telescope». In: *Phys. Rev. D* 98 (8 2018), p. 084063. DOI: 10.1103/PhysRevD.98.084063. URL: <https://link.aps.org/doi/10.1103/PhysRevD.98.084063>.
- [54] F. S. Guzmán and J. M. Rueda-Becerril. «Spherical boson stars as black hole mimickers». In: *Phys. Rev. D* 80 (8 2009), p. 084023. DOI: 10.1103/PhysRevD.80.084023. URL: <https://link.aps.org/doi/10.1103/PhysRevD.80.084023>.
- [55] Amiram Harten, Peter D. Lax, and Bram Van Leer. «On Upstream Differencing and Godunov-Type Schemes for Hyperbolic Conservation Laws». In: *SIAM Review* 25.1 (1983), pp. 35–61. ISSN: 00361445. URL: <http://www.jstor.org/stable/2030019>.
- [56] J. B. Hartle and K. S. Thorne. «Slowly rotating relativistic stars. II. Models for neutron stars and supermassive stars». In: *The Astrophysical Journal* 153.807 (1968). DOI: 10.1086/149707.
- [57] John F. Hawley and Charles R. Evans. «“Constraint preserving transport for magnetohydrodynamics”». In: *Frontiers in numerical relativity* (1989), pp. 179–193.
- [58] Scott H. Hawley and Mathew W. Choptuik. «Boson stars driven to the brink of black hole formation». In: *Phys. Rev. D* 62 (10 Oct. 2000), p. 104024. DOI: 10.1103/PhysRevD.62.104024.
- [59] Carlos A.R. Herdeiro et al. «The imitation game: Proca stars that can mimic the Schwarzschild shadow». In: *Journal of Cosmology and Astroparticle Physics* 2021.04 (2021), p. 051. DOI: 10.1088/1475-7516/2021/04/051.
- [60] David Hilditch and Andreas Schoepe. «Hyperbolicity of divergence cleaning and vector potential formulations of general relativistic magnetohydrodynamics». In: *Phys. Rev. D* 99 (10 May 2019), p. 104034. DOI: 10.1103/PhysRevD.99.104034.
- [61] M. P. Hobson, G. P. Efstathiou, and A. N. Lasenby. *General relativity: An introduction for physicists*. 2006.
- [62] Xiangyu Y. Hu, Nikolaus A. Adams, and Chi-Wang Shu. «Positivity-preserving method for high-order conservative schemes solving compressible Euler equations». In: *Journal of Computational Physics* 242 (2013), pp. 169–180. ISSN: 0021-9991. DOI: <https://doi.org/10.1016/j.jcp.2013.01.024>.
- [63] SETSUO Ichimaru. «Bimodal behavior of accretion disks-Theory and application to Cygnus X-1 transitions». In: *The Astrophysical Journal* 214 (1977), pp. 840–855.
- [64] Phillippe Jetzer. «Boson stars». In: *physrep* 220.4 (Nov. 1992), pp. 163–227. DOI: 10.1016/0370-1573(92)90123-H.

- [65] Nathan K. Johnson-McDaniel et al. «Constraining black hole mimickers with gravitational wave observations». In: *Phys. Rev. D* 102 (12 2020), p. 123010. DOI: 10.1103/PhysRevD.102.123010. URL: <https://link.aps.org/doi/10.1103/PhysRevD.102.123010>.
- [66] Haroldo C. D. Lima Junior et al. «Can different black holes cast the same shadow?». In: *Phys. Rev. D* 103 (8 Apr. 2021), p. 084040. DOI: 10.1103/PhysRevD.103.084040.
- [67] Menou K., Quataert E., and Narayan R. «Astrophysical evidence for black hole event horizons». In: *Recent Developments in Theoretical and Experimental General Relativity, Gravitation, and Relativistic Field Theories*. World Scientific Publishers, 1999, p. 204.
- [68] Eiji KANEDA. «On the Gauss-Codazzi equations». In: *Hokkaido Mathematical Journal* 19.2 (1990), pp. 189–213.
- [69] Rony Keppens et al. «MPI-AMRVAC: A parallel, grid-adaptive PDE toolkit». In: *Computers & Mathematics with Applications* 81 (2021), pp. 316–333. ISSN: 0898-1221. DOI: <https://doi.org/10.1016/j.camwa.2020.03.023>.
- [70] S. I. Kruglov. «The shadow of M87 black hole within rational nonlinear electrodynamics». In: *Modern Physics Letters A* 35.35 (2020), p. 2050291. DOI: 10.1142/S0217732320502910. eprint: <https://doi.org/10.1142/S0217732320502910>. URL: <https://doi.org/10.1142/S0217732320502910>.
- [71] C. Y. Kuo et al. «MEASURING MASS ACCRETION RATE ONTO THE SUPERMASSIVE BLACK HOLE IN M87 USING FARADAY ROTATION MEASURE WITH THE SUBMILLIMETER ARRAY». In: *The Astrophysical Journal* 783.2 (2014), p. L33. DOI: 10.1088/2041-8205/783/2/L33.
- [72] Thomas Lacroix et al. «Unique probe of dark matter in the core of M87 with the Event Horizon Telescope». In: *Phys. Rev. D* 96 (6 2017), p. 063008. DOI: 10.1103/PhysRevD.96.063008. URL: <https://link.aps.org/doi/10.1103/PhysRevD.96.063008>.
- [73] Lacroix, T. and Silk, J. «Constraining the distribution of dark matter at the Galactic centre using the high-resolution Event Horizon Telescope». In: *A&A* 554 (2013), A36. DOI: 10.1051/0004-6361/201220753. URL: <https://doi.org/10.1051/0004-6361/201220753>.
- [74] Jean-Pierre Lasota. «Physics of accretion flows around compact objects». In: *Comptes Rendus Physique* 8.1 (2007). Observation of black holes and extreme gravitational events, pp. 45–56. ISSN: 1631-0705. DOI: <https://doi.org/10.1016/j.crhy.2006.11.002>.
- [75] José P. S. Lemos and Oleg B. Zaslavskii. «Black hole mimickers: Regular versus singular behavior». In: *Phys. Rev. D* 78 (2 2008), p. 024040. DOI: 10.1103/PhysRevD.78.024040. URL: <https://link.aps.org/doi/10.1103/PhysRevD.78.024040>.

- [76] C.D. Levermore. «Relating Eddington factors to flux limiters». In: *Journal of Quantitative Spectroscopy and Radiative Transfer* 31.2 (1984), pp. 149–160. ISSN: 0022-4073. DOI: [https://doi.org/10.1016/0022-4073\(84\)90112-2](https://doi.org/10.1016/0022-4073(84)90112-2).
- [77] Alcubierre M. *Introduction to 3+1 Numerical Relativity*. Oxford Science Publications, 2008.
- [78] Michele Maggiore. *Gravitational Waves. Vol. 1: Theory and Experiments*. Oxford Master Series in Physics. Oxford University Press, 2007.
- [79] Michele Maggiore. *Gravitational Waves. Vol. 2: Astrophysics and Cosmology*. Oxford University Press, Mar. 2018.
- [80] Daniel P. Marrone et al. «An Unambiguous Detection of Faraday Rotation in Sagittarius A». In: *The Astrophysical Journal* 654.1 (2006), pp. L57–L60. DOI: 10.1086/510850.
- [81] E. Massa. «Space tensors in general relativity I: Spatial tensor algebra and analysis». In: *Gen Relat Gravit* 5 (1974), pp. 555–572.
- [82] E. Massa. «Space tensors in general relativity II: Physical applications». In: *Gen Relat Gravit* 5 (1974), pp. 573–591.
- [83] Michael M. May and Richard H. White. «Hydrodynamic Calculations of General-Relativistic Collapse». In: *Phys. Rev.* 141 (4 Jan. 1966), pp. 1232–1241. DOI: 10.1103/PhysRev.141.1232.
- [84] Jacopo Mazza, Edgardo Franzin, and Stefano Liberati. «A novel family of rotating black hole mimickers». In: *Journal of Cosmology and Astroparticle Physics* 2021.04 (Apr. 2021), p. 082. DOI: 10.1088/1475-7516/2021/04/082.
- [85] Jonathan C. McKinney and Charles F. Gammie. «A Measurement of the Electromagnetic Luminosity of a Kerr Black Hole». In: *The Astrophysical Journal* 611.2 (2004), pp. 977–995. DOI: 10.1086/422244.
- [86] Z Meliani et al. «Circular geodesics and thick tori around rotating boson stars». In: *Classical and Quantum Gravity* 32.23 (Nov. 2015), p. 235022. DOI: 10.1088/0264-9381/32/23/235022.
- [87] F. Curtis Michel. «Accretion of Matter by Condensed Objects». In: *Astrophysics and Space Sciences* 15.1 (Jan. 1972), pp. 153–160. DOI: 10.1007/BF00649949.
- [88] Charles W. Misner, K. S. Thorne, and J. A. Wheeler. *Gravitation*. W. H. Freeman, 1973.
- [89] J. M. Moran, L. J. Greenhill, and J. R. Herrnstein. «Observational evidence for massive black holes in the centers of active galaxies». In: *J. Astrophys. Astron.* 20 (1999), pp. 165–185. DOI: 10.1007/BF02702350.
- [90] Kamal K. Nandi et al. «Ring-down gravitational waves and lensing observables: How far can a wormhole mimic those of a black hole?». In: *Phys. Rev. D* 95 (10 2017), p. 104011. DOI: 10.1103/PhysRevD.95.104011. URL: <https://link.aps.org/doi/10.1103/PhysRevD.95.104011>.

- [91] Ramesh Narayan, Igor V. Igumenshchev, and Marek A. Abramowicz. «Magnetically Arrested Disk: an Energetically Efficient Accretion Flow». In: *Publications of the Astronomical Society of Japan* 55.6 (Dec. 2003), pp. L69–L72. ISSN: 0004-6264. DOI: 10.1093/pasj/55.6.L69.
- [92] Ramesh Narayan, Michael D. Johnson, and Charles F. Gammie. «The Shadow of a Spherically Accreting Black Hole». In: *The Astrophysical Journal* 885.2 (Nov. 2019), p. L33. DOI: 10.3847/2041-8213/ab518c.
- [93] Ramesh Narayan et al. «GRMHD simulations of magnetized advection-dominated accretion on a non-spinning black hole: role of outflows». In: *Monthly Notices of the Royal Astronomical Society* 426.4 (Nov. 2012), pp. 3241–3259. ISSN: 0035-8711. DOI: 10.1111/j.1365-2966.2012.22002.x.
- [94] Scott C. Noble et al. «Primitive Variable Solvers for Conservative General Relativistic Magnetohydrodynamics». In: *The Astrophysical Journal* 641.1 (2006), pp. 626–637. DOI: 10.1086/500349.
- [95] I. D. Novikov and K. S. Thorne. «Astrophysics and black holes». In: *Les Houches Summer School of Theoretical Physics: Black Holes*. 1973, pp. 343–550.
- [96] Hector Olivares et al. «How to tell an accreting boson star from a black hole». In: *Mon. Not. Roy. Astron. Soc.* 497.1 (2020), pp. 521–535. DOI: 10.1093/mnras/staa1878. arXiv: 1809.08682 [gr-qc].
- [97] J. R. Oppenheimer and G. M. Volkoff. «On Massive Neutron Cores». In: *Phys. Rev.* 55 (4 Feb. 1939), pp. 374–381. DOI: 10.1103/PhysRev.55.374.
- [98] Carlos Palenzuela. «Introduction to Numerical Relativity». In: *Frontiers in Astronomy and Space Sciences* 7 (2020), p. 58. DOI: 10.3389/fspas.2020.00058.
- [99] Philippos Papadopoulos and José A. Font. «Relativistic hydrodynamics on spacelike and null surfaces: Formalism and computations of spherically symmetric spacetimes». In: *Phys. Rev. D* 61 (2 Dec. 1999), p. 024015. DOI: 10.1103/PhysRevD.61.024015.
- [100] Arlie Petters, Harold Levine, and Joachim Wambsganss. *Singularity Theory and Gravitational Lensing*. Birkhäuser Basel, Mar. 2001.
- [101] Matthew Pitkin et al. «Gravitational Wave Detection by Interferometry (Ground and Space)». In: *Living Rev. Rel.* 14 (2011), p. 5. DOI: 10.12942/lrr-2011-5.
- [102] Oliver Porth et al. «The Event Horizon General Relativistic Magnetohydrodynamic Code Comparison Project». In: *Astrophys. J. Suppl.* 243.2 (2019), p. 26. DOI: 10.3847/1538-4365/ab29fd. arXiv: 1904.04923 [astro-ph.HE].
- [103] Oliver Porth et al. «The Black Hole Accretion Code». In: *Computational Astrophysics and Cosmology* 4 (1 Nov. 2016). DOI: 10.1186/s40668-017-0020-2.

- [104] J.E. Pringle. «Accretion discs in Astrophysics». In: *Ann. Rev. Astron. Astrophys.* 19 (1981).
- [105] David Radice, Luciano Rezzolla, and Filippo Galeazzi. «High-order fully general-relativistic hydrodynamics: new approaches and tests». In: *Classical and Quantum Gravity* 31.7 (2014), p. 075012. DOI: 10.1088/0264-9381/31/7/075012.
- [106] L. Rezzolla and O. Zanotti. *Relativistic Hydrodynamics*. Oxford University Press, 2013.
- [107] Luciano Rezzolla and Alexander Zhidenko. «New parametrization for spherically symmetric black holes in metric theories of gravity». In: *Phys. Rev. D* 90 (8 2014), p. 084009. DOI: 10.1103/PhysRevD.90.084009.
- [108] R. D. Richtmyer and K. W. Morton. *Difference Methods for Initial Value Problems*. Krieger Pub Co., 1994.
- [109] Markus Rummel and C. P. Burgess. «Constraining Fundamental Physics with the Event Horizon Telescope». In: *JCAP* 05 (2020), p. 051. DOI: 10.1088/1475-7516/2020/05/051. arXiv: 2001.00041 [gr-qc].
- [110] Aleksander Sadowski et al. «Numerical simulations of super-critical black hole accretion flows in general relativity». In: *Monthly Notices of the Royal Astronomical Society* 439.1 (Jan. 2014), pp. 503–520. DOI: 10.1093/mnras/stt2479.
- [111] Aleksander Sadowski et al. «Semi-implicit scheme for treating radiation under M1 closure in general relativistic conservative fluid dynamics codes». In: *Monthly Notices of the Royal Astronomical Society* 429.4 (Jan. 2013), pp. 3533–3550. ISSN: 0035-8711. DOI: 10.1093/mnras/sts632.
- [112] N. Sanchis-Gual et al. «Nonlinear Dynamics of Spinning Bosonic Stars: Formation and Stability». In: *Phys. Rev. Lett.* 123 (22 Nov. 2019), p. 221101. DOI: 10.1103/PhysRevLett.123.221101.
- [113] Nicolas Sanchis-Gual et al. «Numerical evolutions of spherical Proca stars». In: *Phys. Rev. D* 95 (10 May 2017), p. 104028. DOI: 10.1103/PhysRevD.95.104028.
- [114] William E. Schiesser and Graham W. Griffiths. *A Compendium of Partial Differential Equation Models: Method of Lines Analysis with Matlab*. Cambridge University Press, 2009. DOI: 10.1017/CB09780511576270.
- [115] Franz E. Schunck and Eckehard W. Mielke. «General relativistic boson stars». In: *Class. Quant. Grav.* 20 (2003), R301–R356. DOI: 10.1088/0264-9381/20/20/201. arXiv: 0801.0307 [astro-ph].
- [116] B F Schutz. «Gravitational-wave sources». In: *Classical and Quantum Gravity* 13.11A (Nov. 1996), A219–A238. DOI: 10.1088/0264-9381/13/11a/031.
- [117] F. H. Seguin. «The stability of nonuniform rotation in relativistic stars.» In: *Astrophys. J.* 197 (May 1975), pp. 745–765. DOI: 10.1086/153563.

- [118] Edward Seidel and Wai-Mo Suen. «Dynamical evolution of boson stars: Perturbing the ground state». In: *Phys. Rev. D* 42 (2 July 1990), pp. 384–403. DOI: 10.1103/PhysRevD.42.384.
- [119] Edward Seidel and Wai-Mo Suen. «Formation of solitonic stars through gravitational cooling». In: *Phys. Rev. Lett.* 72 (16 Apr. 1994), pp. 2516–2519. DOI: 10.1103/PhysRevLett.72.2516.
- [120] N. I. Shakura and R. A. Sunyaev. «Black holes in binary systems. Observational appearance.» In: *Astronomy & Astrophysics* 500 (June 1973), pp. 33–51.
- [121] S. L. Shapiro, A. P. Lightman, and D. M. Eardley. «A two-temperature accretion disk model for Cygnus X-1: structure and spectrum.» In: *Astrophysical Journal* 204 (Feb. 1976), pp. 187–199. DOI: 10.1086/154162.
- [122] Masaru Shibata and Takashi Nakamura. «Evolution of three-dimensional gravitational waves: Harmonic slicing case». In: *Phys. Rev. D* 52 (10 Nov. 1995), pp. 5428–5444. DOI: 10.1103/PhysRevD.52.5428.
- [123] Hotaka Shiokawa. «General-relativistic magnetohydrodynamics simulations of black hole accretion disks: Dynamics and radiative properties». PhD thesis. University of Illinois at Urbana-Champaign, 2013.
- [124] Larry Smarr and James W. York. «Kinematical conditions in the construction of spacetime». In: *Phys. Rev. D* 17 (10 1978), pp. 2529–2551. DOI: 10.1103/PhysRevD.17.2529.
- [125] James M. Stone et al. «The Athena++ Adaptive Mesh Refinement Framework: Design and Magnetohydrodynamic Solvers». In: *The Astrophysical Journal Supplement Series* 249.1 (2020), p. 4. DOI: 10.3847/1538-4365/ab929b.
- [126] Sergey P. Tarabrin. «Interaction of plane gravitational waves with a Fabry-Perot cavity in the local Lorentz frame». In: *Phys. Rev. D* 75 (10 May 2007), p. 102002. DOI: 10.1103/PhysRevD.75.102002.
- [127] Matheus C. Teodoro, Lucas G. Collodel, and Jutta Kunz. «Retrograde polish doughnuts around boson stars». In: *Journal of Cosmology and Astroparticle Physics* 2021.03 (Mar. 2021), p. 063. DOI: 10.1088/1475-7516/2021/03/063.
- [128] Richards Thompson, James Moran, and George Swenson Jr. *Interferometry and Synthesis in Radio Astronomy*. Springer International Publishing, Mar. 2017.
- [129] K. S. Thorne and D. MacDonald. «Electrodynamics in Curved Spacetime - 3+1 Formulation». In: *mnras* 198 (Jan. 1982), p. 339. DOI: 10.1093/mnras/198.2.339.
- [130] Eleuterio F. Toro. *Riemann Solvers and Numerical Methods for Fluid Dynamics*. 3rd Edition. Springer-Verlag Berlin Heidelberg, 2009.

- [131] Alexandre Toubiana et al. «Modeling gravitational waves from exotic compact objects». In: *Phys. Rev. D* 103 (6 2021), p. 064042. DOI: 10.1103/PhysRevD.103.064042. URL: <https://link.aps.org/doi/10.1103/PhysRevD.103.064042>.
- [132] Bram van Leer. «Towards the ultimate conservative difference scheme. V. A second-order sequel to Godunov's method». In: *Journal of Computational Physics* 32.1 (1979), pp. 101–136. ISSN: 0021-9991. DOI: [https://doi.org/10.1016/0021-9991\(79\)90145-1](https://doi.org/10.1016/0021-9991(79)90145-1).
- [133] F H Vincent et al. «Imaging a boson star at the Galactic center». In: *Classical and Quantum Gravity* 33.10 (Apr. 2016), p. 105015. DOI: 10.1088/0264-9381/33/10/105015.
- [134] Robert M. Wald. *General Relativity*. Chicago, USA: Chicago Univ. Pr., 1984. DOI: 10.7208/chicago/9780226870373.001.0001.
- [135] James W. York Jr. «Kinematics and Dynamics of General Relativity». In: *Workshop on Sources of Gravitational Radiation*. 1978.
- [136] Shijun Yoshida and Yoshiharu Eriguchi. «Rotating boson stars in general relativity». In: *Phys. Rev. D* 56 (2 July 1997), pp. 762–771. DOI: 10.1103/PhysRevD.56.762.
- [137] Feng Yuan and Ramesh Narayan. «Hot Accretion Flows Around Black Holes». In: *Annual Review of Astronomy and Astrophysics* 52.1 (2014), pp. 529–588. DOI: 10.1146/annurev-astro-082812-141003.